

AD-A039 497

SPERRY RESEARCH CENTER SUDBURY MASS
MULTIPLE FREQUENCY CLASSIFICATION TECHNIQUE. (U)

MAR 77 J P TOOMEY, C L BENNETT

F30602-76-C-0039

NL

UNCLASSIFIED

RADC-TR-77-120

F/6 17/9

1 OF 1
AD
A039497



END

DATE
FILED
16-77

ADA 039497

RADC-TR-77-120
Final Technical Report
March 1977

12



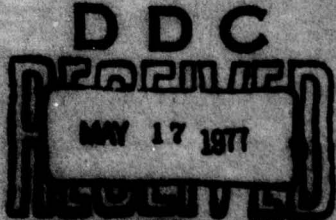
MULTIPLE FREQUENCY CLASSIFICATION TECHNIQUE

Sperry Research Center

Approved for public release; distribution unlimited.

AD No.
DDC FILE COPY

RAFLE AIR DEVELOPMENT CENTER
AIR FORCE SYSTEMS COMMAND
GRIFFITHS AIR FORCE BASE, NEW YORK 13441



This report has been reviewed by the RADC Information Office (OI) and is releasable to the National Technical Information Service (NTIS). At NTIS it will be releasable to the general public including foreign nations.

This report has been reviewed and is approved for publication.

APPROVED:

Daniel L. Tauroney
DANIEL L. TAURONEY
Project Engineer

APPROVED:

Joseph L. Ryerson
JOSEPH L. RYERSON
Technical Director
Surveillance Division

FOR THE COMMANDER:

John P. Huss
JOHN P. HUSS
Acting Chief, Plans Office

Do not return this copy. Retain or destroy.

UNCLASSIFIED

SECURITY CLASSIFICATION OF THIS PAGE (When Data Entered)

REPORT DOCUMENTATION PAGE		READ INSTRUCTIONS BEFORE COMPLETING FORM
1. REPORT NUMBER RADCR-TR-77-120	2. GOVT ACCESSION NO.	3. RECIPIENT'S CATALOG NUMBER 9
4. TITLE (and subtitle) MULTIPLE FREQUENCY CLASSIFICATION TECHNIQUE		5. TIME OF REPORT & PERIOD COVERED Final Technical Report 26 Nov 75 - 30 Nov 76
6. AUTHOR(s) J. P. Toomey C. L. Bennett		7. PERFORMING ORG. REPORT NUMBER N/A
8. PERFORMING ORGANIZATION NAME AND ADDRESS Sperry Research Center 100 North Road Sudbury MA 01776		9. PROGRAM ELEMENT, PROJECT, TASK AREA & WORK UNIT NUMBERS 62702F 43060574
10. CONTROLLING OFFICE NAME AND ADDRESS Rome Air Development Center (OCTM) Griffiss AFB NY 13441		11. REPORT DATE Mar 1977
12. MONITORING AGENCY NAME & ADDRESS (if different from Controlling Office) Same		13. NUMBER OF PAGES 86
14. DISTRIBUTION STATEMENT (of this Report) Approved for public release; distribution unlimited.		15. SECURITY CLASS. (of this report) UNCLASSIFIED
16. DECLASSIFICATION/DOWNGRADING SCHEDULE N/A		17. DISTRIBUTION STATEMENT (of the abstract entered in Block 20, if different from Report) Same
18. SUPPLEMENTARY NOTES RADC Project Engineer: Daniel L. Tauroney (OCTM) 408 199		
19. KEY WORDS (Continue on reverse side if necessary and identify by block number) Target Classification Decision Theoretic Principles Collocated Radars Aspect Angle		
20. ABSTRACT (Continue on reverse side if necessary and identify by block number) The overall objective of this study was to develop a method for the shape classification of space objects using data from two or more collocated radars operating at different frequencies. The basic technique consists of appropriately comparing the received radar data with the contents of a stored signature library which is obtained with the Space-Time Integral Equation (STIE) method for calculating the exact impulse response (or entire frequency response) of conducting bodies.		

6/2

UNCLASSIFIED

SECURITY CLASSIFICATION OF THIS PAGE (When Data Entered)

The target classification algorithm was developed from statistical decision theoretic principles as opposed to the more typical (and Heuristic) pattern recognition approach. This viewpoint, coupled with the rigorous STIE technique provides a means for reliable classification of objects during the first revolution. The results described in this document show that essentially error-free, real time classification be achieved (with existing radars and only two frequencies) well before the point of closest approach of the target on the first pass in view of the radars. The classification technique requires no prior information concerning target motion (aspect angle): the target aspect angle is estimated automatically. The algorithm operates sequentially on the incoming data so that no radar data storage is required. In addition, the classifier can reliably determine if the target is an unknown object (not in the signature library) by means of its target rejection capability. After each radar observation is processed, a measure of the confidence associated with the current decision is computed. This credence parameter could enable the earliest possible classification with a pre-specified acceptable error rate.

UNCLASSIFIED

SECURITY CLASSIFICATION OF THIS PAGE (When Data Entered)

TABLE OF CONTENTS

<u>Section</u>		<u>Page</u>
1	INTRODUCTION	1
2	ASSUMED TARGET SET	4
	2.1 Target Shape and Size	4
	2.2 Frequency Space Trajectories	4
	2.3 The Frequency Space Trajectory File	6
3	THE FREQUENCY SPACE TRAJECTORY CLASSIFIER	11
	3.1 Basic Radar Site Configuration	11
	3.2 Technical Approach to Classifier Development	11
	3.3 The Likelihood Measure of Closeness	12
	3.4 The Problem of Unknown Aspect	14
	3.5 Aspect Estimation: The Generalized Likelihood Function	15
	3.6 The Generalized Likelihood Classifier for a Single Look	17
	3.7 Classifier Structure for Multiple Observations	17
	3.8 Optimality of the Classifier	20
	3.9 Summary	20
4	TARGET CLASSIFICATION PERFORMANCE	23
	4.1 Horizon Stabilized Vehicles	23
	4.1.1 Orbital Geometry and Aspect Variation	23
	4.1.2 Monte-Carlo Results for Correct Classification Rate	25
	4.1.3 Aspect Estimation Performance	31
	4.2 Earth-Center Stabilized Vehicles	34
	4.3 Tumbling Vehicles	36
	4.4 Summary of Classifier Performance	38
5	A DECISION CONFIDENCE MEASURE	40
	5.1 Description of the Confidence Measure	40
	5.2 Performance of the Decision Confidence Measure	42
6	REJECTION OF UNKNOWN TARGETS	45
	6.1 Description of the Rejection Method	45
	6.2 Test Results for Target Rejection	47
7	A PRELIMINARY EXPERIMENT PLAN	50
	7.1 Radar Site Selection	50

TABLE OF CONTENTS (CONT)

<u>Section</u>		<u>Page</u>
7.2	Target Set Selection	51
7.2.1	Target Shape and Size	51
7.2.2	Target Dynamical Motion	52
7.3	Specific Data Requirements	53
7.4	Ionosphere Effects	55
8	SUMMARY AND CONCLUSIONS	56
9	REFERENCES	58
10	APPENDICES	61
10.1	The Space-Time Integral Equation Method	61
10.1.1	Space-Time Integral Equation Solution	62
10.1.2	Impulse Response Augmentation Technique	64
10.1.3	Application to Prolate Spheroid and Sphere-Capped Cylinder	65
10.2	Statistics of the RCS Measurements	68
10.3	Details of the Likelihood Functions	71

LIST OF ILLUSTRATIONS

<u>Figure</u>	<u>Page</u>
1 Target Shape and Size	5
2 Frequency Space Trajectories at VHF, UHF	7
3 Frequency Space Trajectories at L and S Bands	8
4 FST at L, S Bands With One Degree Aspect Increment	10
5 Illustrating the Likelihood Classifier	13
6 The Geometry of Aspect Estimation	16
7 The Generalized Likelihood Classifier for a Single Look	18
8 The Generalized Likelihood Classifier for Multiple Observations	21
9 Parameters for a Circular Orbit	24
10 Range and Aspect Variation During Pass of Horizon Stabilized Vehicle	26
11 Apparent Noisy RCS at 155.5 MHz (ALTAIR - VHF)	27
12 Apparent Noisy RCS at 415 MHz (ALTAIR - UHF)	28
13 Classification Performance for Horizon Stabilized Targets	30
14 Classification Performance, $N_a = 100$	32
15 Estimated Aspect for Orbiting Prolate Spheroid	33
16 Aspect Variation for ECS Vehicles	35
17 Classification Performance: Tumbling Targets	37
18 Illustrating the Probability Densities of the Classifier Outputs after N Observations When H_k is True	41
19 Performance of the Confidence Measure	43
20 Probability Considerations for the Reject Method	46
21 Approximate Frequency Space Trajectories Right Circular Cylinder	48
22 Performance of Rejection Confidence Measure	49
23 Observation Rate Limitations for Tumbling Targets	54
24 Geometries of Targets for Signature Library	66
25 Model of Radar Receiver	69
26 Signal to Noise Ratio for One Square Meter Target	74

EVALUATION

The Air Force sought an approach to combining the output of two different collocated radars as a method for classifying space targets while being observed at the same aspect angle. Sperry Research Corporation (SRC) developed an algorithm and an experiment designed to accomplish the classification on two simple space targets. The statistical decision principle appears to be an excellent approach to solving this classification problem. This approach has been highly recommended to the space object identification community and should prove useful for future Air Force systems.

Daniel L. Tauroney
DANIEL L. TAURONEY
Project Engineer

SECTION 1

INTRODUCTION

This document is submitted as the final report in response to the requirements set forth in Contract No. F30602-76-C-0039 between the Sperry Research Center, Sudbury, Massachusetts and the Air Force Systems Command, Rome Air Development Center, Griffiss Air Force Base, New York. The primary objectives of this program, prosecuted during the period 26 November 1975 through 30 November 1976, were (1) to obtain the general expression for the impulse response of the prolate spheroid and sphere-capped cylinder as a function of arbitrary incident angle and polarization; (2) to generalize the frequency space-trajectory classification technique to include unknown target aspect angle and polarization; (3) to apply these results using the parameters of existing radars to demonstrate the decision process on a sphere, prolate spheroid, and sphere-capped cylinder of comparable size, including the effects of additive noise; and (4) to plan experiments and determine which data would be needed to demonstrate the technique using real satellite data.

The methods used to meet these objectives and the results obtained are unique in several respects. The scattering response calculations were done using the Space-Time Integral Equation (STIE) and impulse response augmentation methods (Appendix 1) which enable the determination of the exact impulse response (or, equivalently, the response at all frequencies) of the target. This approach is particularly beneficial in the difficult resonance region where the radar wavelength is of the order of the size of the target.

The frequency space trajectory classification technique uses the Radar Cross Section (RCS) results computed with the STIE method to decide which target in the signature library is best represented by the observed radar data. In contrast to some other studies [1,2,3], a statistical hypothesis testing, rather than pattern recognition, approach was the basis for the classification technique. As discussed in Appendix 2, this viewpoint required a statistical model of the effect of radar receiver noise on the

RCS measurements made by radars. The parameters of the ALTAIR [4] and TRADEX [5] radars were used to specify the statistical distributions of the data input to the classifier because these radars are likely candidates for an experimental test of the method (Section 7).

The generalized likelihood classifier developed under this contract has several advantages over those described in previously published work [1,2,3]. It requires modifications to only the data-processing portions of existing radars and therefore would be a relatively simple add-on to operational sites with a multifrequency capability. The classifier requires absolutely no prior information (statistical or deterministic) concerning target aspect or dynamical motion. As indicated in Section 3, aspect estimation is an automatic "by-product" of the operation of the classifier. This feature could be used to measure target motion or detect sudden changes in target attitude.

The classifier operates sequentially in time on the received radar data. No storage of radar data is required but the decision at a given time is dependent on all the data received up to and including that time. The decision statistic is updated after each observation is received. A measure of the confidence to be associated with the current decision is also computed. The classifier structure thus enables very early target classification depending on the desired decision confidence. The simulation studies done for this contract show that only a small number of radar observations (at only two frequencies) during the early portion of the first pass of either stable or tumbling objects are required for essentially error-free shape classification.

An additional attractive feature of this classification method is the capability to recognize that the target being tracked is not closely represented by any of the targets in the signature library. This is the target reject confidence described in Section 6.

Section 2 discusses the shape, size, and radar cross section of the targets assumed for this study. A description of the philosophy and operation of the classification technique is given in Section 3. Section 4

presents the results of Monte Carlo simulations to determine the correct classification rate for both stabilized and tumbling vehicles. The design and operation of the decision confidence and rejection algorithms are described in Sections 5 and 6, respectively. The considerations which must be addressed in order to conduct a cost-effective field test of the method are outlined in Section 7. Section 8 contains a brief summary, the major conclusions of the study, and some promising directions for future work in addition to the experimental test. The appendices (Section 10) include a description of the Space-Time Integral Equation method, the detailed mathematical formulas for the probability distributions of the radar data and the likelihood functions used by the classification algorithm.

SECTION 2 ASSUMED TARGET SET

In this section we discuss the target shapes assumed for the study and the representation of these shapes in terms of their RCS at different frequencies, polarizations, and aspect angles. This representation is a key element in understanding the classification algorithm.

2.1 TARGET SHAPE AND SIZE

In accordance with the objectives of the contract, the target shapes that were investigated are shown in Figure 1. They are a sphere, a prolate spheroid, and a sphere-capped cylinder of similar size. Note that the prolate spheroid and sphere-capped cylinder have the same length. The axial projected area of the prolate spheroid is the same as that for the sphere. The elements of the linear polarization scattering matrix [6] for all aspects and frequencies (dc to optics) were computed for these targets using the space time integral equation method (Appendix 10.1). The results of these calculations are described in the next section.

2.2 FREQUENCY SPACE TRAJECTORIES

Since the ALTAIR and TRADEX radars operate with circular polarization, only the circular polarization radar cross section is considered here. This has the additional benefit of eliminating any explicit dependence of the radar cross section on the polarization vector orientation with respect to the target axis, thus enabling cost-effective classification processing. These radars transmit right-hand circular polarization (RHCP) and will see the sphere only in the left-hand circular polarization (LHCP) receiving channel. The numerical results given here apply to radars which transmit and receive opposite sense polarizations, but the classification software is set up to handle dual receive polarizations (RHCP and LHCP) at multiple frequencies.

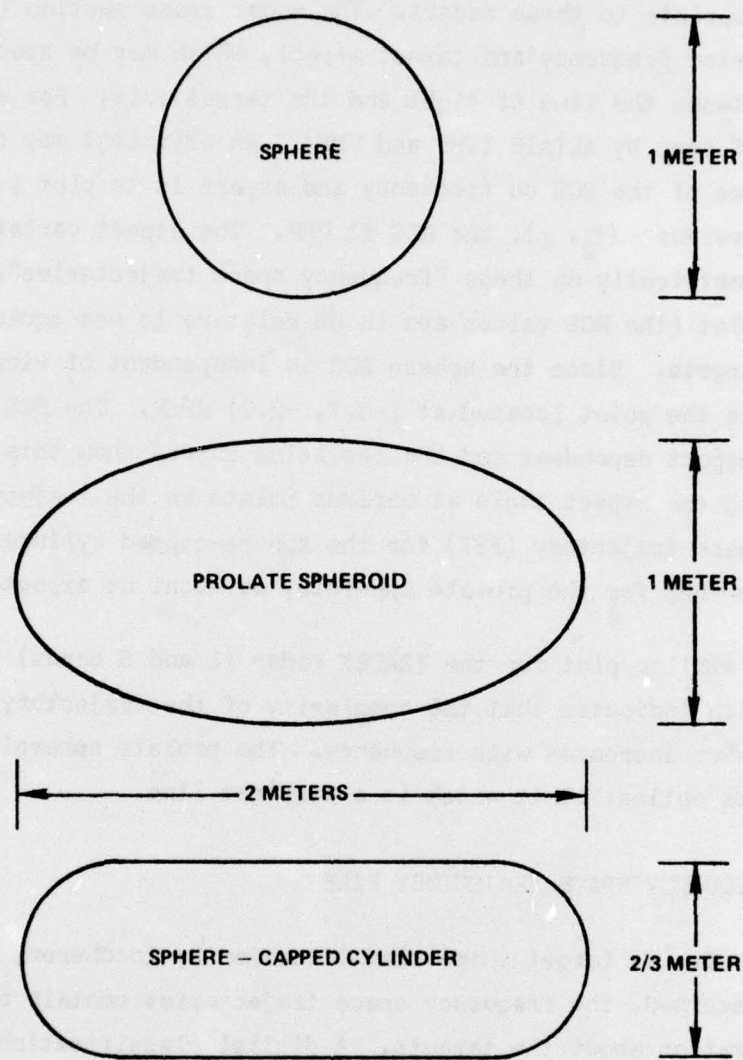


FIG. 1 Target Shape and Size

With the circular polarization condition specified, the linear polarization scattering matrix can be used to calculate the radar cross section appropriate to these radars. The radar cross section (RCS) depends on radar carrier frequency and target aspect, which may be specified as the angle, ϕ , between the line of sight and the target axis. For example, consider the RCS seen by ALTAIR (VHF and UHF). An efficient way of displaying the dependence of the RCS on frequency and aspect is to plot $\sigma(f_1, \phi)$, the RCS at VHF, versus $\sigma(f_2, \phi)$, the RCS at UHF. The aspect variation then appears parametrically on these "frequency space trajectories". Figure 2 shows this plot (the RCS values are in dB relative to one square meter) for the three targets. Since the sphere RCS is independent of viewing angle, it appears as the point located at (-3.7, -2.0) dBsm. The RCS of the other targets is aspect dependent and the resulting curves show this dependence by indicating the aspect angle at various points on the trajectory. The frequency space trajectory (FST) for the sphere-capped cylinder is more complex than that for the prolate spheroid, as might be expected.

A similar plot for the TRADEX radar (L and S bands) is shown in Figure 3 which indicates that the complexity of the trajectory for the sphere capped cylinder increases with frequency. The prolate spheroid FST is approaching its optical limit which is a straight line.

2.3 THE FREQUENCY SPACE TRAJECTORY FILE

As far as target shape classification by incoherent radar measurements is concerned, the frequency space trajectories contain all possible prior information about the targets. A digital classification processor must have a stored (sampled) representation of these curves. The stored RCS values are indexed by target, frequency, receive polarization, and aspect. A comparison of Figures 2 and 3 indicates that the variation of target RCS with aspect increases greatly with frequency. This implies that using the higher frequencies demands much greater storage allocation than at the lower frequencies. The aspect increment on the plots in Figure 2 is one degree, while the aspect increment in Figure 3 is one tenth of a degree.

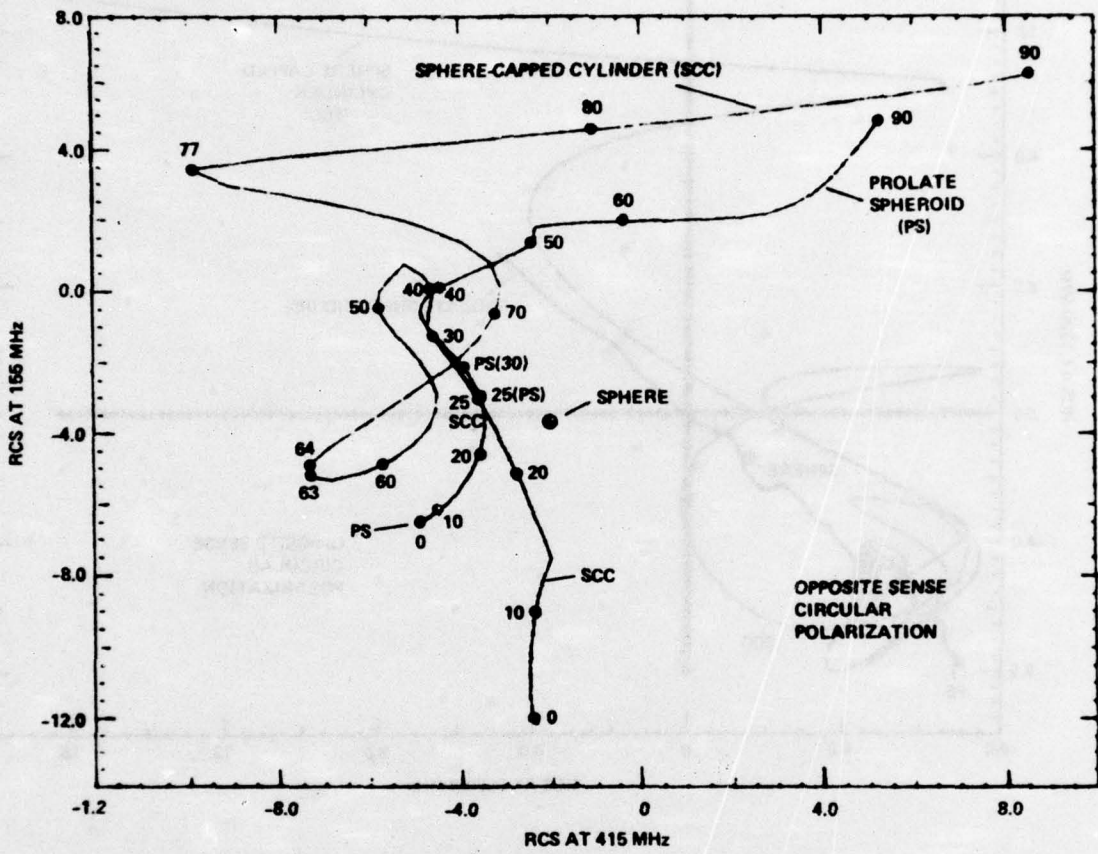


FIG. 2 Frequency Space Trajectories at VHF, UHF

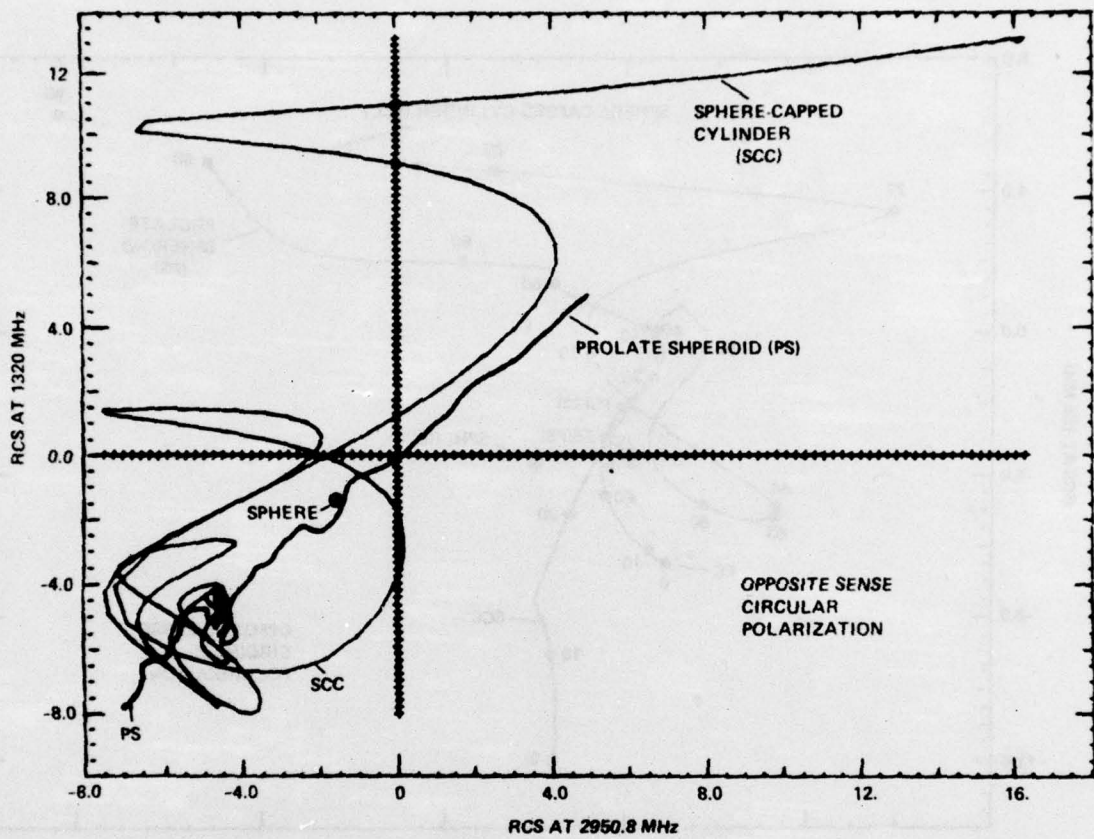


FIG. 3 Frequency Space Trajectories at L and S Bands

The number of storage words required by the FST file is

$$N_T N_f N_p N_\phi$$

where

N_T = number of targets

N_f = number of frequencies

N_p = number of polarizations (one or two)

N_ϕ = number of aspects

The numerical results for this report are based on $N_T = 3$, $N_f = 4$, $N_p = 1$ (receive LHCP), and $N_\phi = 90$ (one degree aspect increment) so that the file contains 360 words per target or 1080 words. The one degree aspect increment provides a more than adequate representation of the RCS at VHF and UHF but is somewhat coarse at the higher frequencies (especially at S-band). Figure 4 shows the frequency space trajectories at L and S bands with a one degree aspect increment. Jumps of several dB between points are evident. The effect of an undersampled (in aspect) frequency space trajectory file is discussed in subsequent sections of this report. There is clearly a tradeoff between processing resource requirements and classification performance involved. It is emphasized that no detailed study of this tradeoff has been done: this is properly the subject of a separate study. The parameters assumed here are reasonable choices which enable a general assessment of the major benefits and limitations of the frequency space trajectory target classification method.

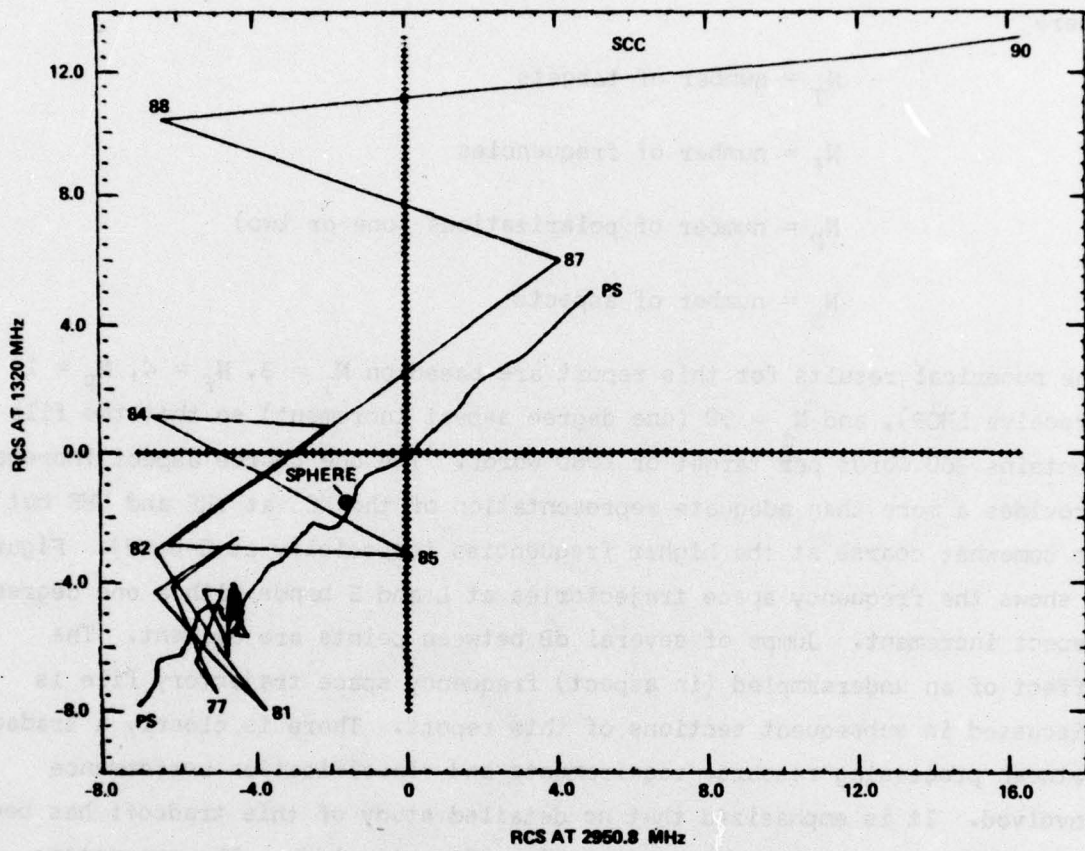


FIG. 4 FST at L, S Bands With One Degree Aspect Increment

SECTION 3

THE FREQUENCY SPACE TRAJECTORY CLASSIFIER

This section describes the basic algorithmic structure of the generalized likelihood target classifier. The mathematical details are given in Appendices 10.2 and 10.3.

3.1 BASIC RADAR SITE CONFIGURATION

The basic methods developed in this study apply to radar sites which are capable of measuring the radar cross section (received signal amplitude) of orbiting vehicles at two or more different frequencies. The radar installation could consist of one multifrequency radar or two collocated radars operating at different frequencies. The use of circular polarization enables much faster target classification because the polarization angle "nuisance parameter" is eliminated. The proximity of the radars must be sufficient to ensure that these radars all see the target at approximately the same aspect angle. The numerical results obtained for this report apply to the ALTAIR and TRADEX radars at the Kwajalein site which is probably the best candidate for a field-data test of the method.

3.2 TECHNICAL APPROACH TO CLASSIFIER DEVELOPMENT

A measurement of target RCS is basically a scaled estimate of received signal power. The scale factor involves the radar system parameters and the range to the target as discussed in Appendix 10.2. A single look or observation of target RCS might be based on one or more pulses (pulse averaging). A single look multifrequency (or multi-polarization) measurement of target RCS by a space surveillance radar installation can be represented mathematically by a vector, Y , of dimension equal to the number of different frequency-polarization pairs used. Thus a single observation at VHF and UHF will appear as a single point the frequency space trajectory plane such as in Figure 2.

The location of this point will depend on the shape and size of the target being illuminated, the aspect angle, and the polarization of the radars. Even under identical conditions (static target), however, the location of the RCS observation vector Y will fluctuate randomly about the true target RCS due to noise effects. The magnitude of these fluctuations will depend on range, RCS, and the parameters of the radar installation (Appendix 10.2). In order to classify targets we then must develop a measure of closeness or distance between the noisy observations and the library RCS data represented in Figures 2 and 3. The classifier would operate by choosing the frequency space trajectory which is closest to the observed data.

3.3 THE LIKELIHOOD MEASURE OF CLOSENESS

Rather than selecting some arbitrary measure of closeness (as is often done in pattern recognition approaches) we have appealed to the powerful techniques of statistical decision theory which indicate that, given an observation, the classifier should choose the target which makes that observation the most likely.

To clarify this idea we consider a highly simplified example. Suppose the observation vector is one dimensional (only single frequency RCS measurements are available) and the aspect angle is known exactly. Suppose further that we wish to decide which one of M possible targets is present and all are equally likely to occur. The M hypotheses which specify this problem can be listed as

Hypothesis 1 (H_1): Target 1 is present

Hypothesis 2 (H_2): Target 2 is present

⋮

Hypothesis M (H_M): Target M is present

Assuming the range is known, the probability distribution (probability density function) of the observation for each hypothesis can be specified. A sketch of the result for $M = 4$ is shown in Figure 5 where the bell-shaped

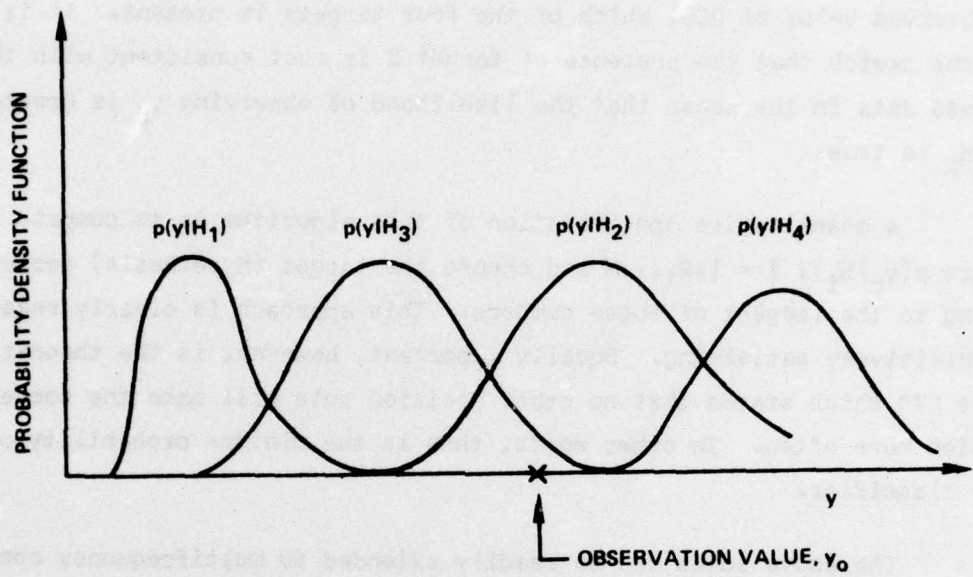


FIG. 5 Illustrating the Likelihood Classifier

curves, $p(y|H_i)$, represent the known probability density function when each hypothesis is true. Let the cross on the abscissa at $y = y_0$ indicate the specific value of the RCS observation by the radar. This picture describes the decision problem confronting the classifier which must decide, based on the observed value of RCS, which of the four targets is present. It is clear from the sketch that the presence of target 2 is most consistent with the observed data in the sense that the likelihood of observing y_0 is greatest when H_2 is true.

A quantitative specification of this algorithm is to compute the numbers $p(y_0|H_i)$; $i = 1, 2, \dots, M$ and choose the target (hypothesis) corresponding to the largest of these numbers. This approach is clearly reasonable and intuitively satisfying. Equally important, however, is the theoretical result [7] which states that no other decision rule will make the correct decision more often. In other words, this is the minimum probability of error classifier.

The above ideas can be readily extended to multifrequency observations. It is clear then, that a theoretically well-founded choice of the measure of proximity between a multifrequency RCS observation Y and the frequency space trajectory corresponding to target i is $p(Y|H_i)$. We shall use the notation $L_i(Y) = p(Y|H_i)$ for these likelihood functions. A large value of L_i means that the observation Y is highly consistent with target i being present.

3.4 THE PROBLEM OF UNKNOWN ASPECT

The discussion of the previous section applied to the situation where target aspect is known. In practice, of course, the aspect is unknown and the likelihood functions are not completely specified so cannot be calculated. Complete specification of the function L_i requires knowledge of the radar system parameters as well as target range and RCS (see Appendix 10.2). Since range can be estimated very accurately, the only unknown parameter determining the likelihood function is target RCS which is dependent on the aspect angle.

Decision problems where the likelihood functions involve an unknown parameter are termed composite. We shall indicate the dependence on the unknown aspect by the notation

$$L_i(Y; \varphi) = p(Y; \varphi | H_i)$$

where φ is the aspect angle. If φ is assumed to be a random variable with a specified probability distribution, the optimum way to proceed [7] is to average out the effect of aspect on the likelihood functions and use the resultant averaged likelihood functions, $\tilde{L}_i(Y)$, in the classifier as above:

$$\tilde{L}_i(Y) = \int L_i(Y; \varphi) p(\varphi) d\varphi \quad (3-1)$$

where $p(\varphi)$ is the assumed density function for the aspect angle. This approach is valid only if reliable prior information about the target aspects which the radar site will encounter is available. Since orbiting vehicles may be either stabilized or tumbling, a complicated stochastic model of aspect variation would be required. Even if this were feasible, evaluation of the integral in (3-1) might be computationally prohibitive.

3.5 ASPECT ESTIMATION: THE GENERALIZED LIKELIHOOD FUNCTION

An alternate approach to the unknown aspect problem is to estimate the target aspect from the observed data, a procedure which has been called the generalized likelihood approach [7]. This technique is best understood with the aid of Figure 6 which illustrates the two-frequency case. The observation is closest to the library data when the aspect for this target is approximately equal to φ_6 . In this case it is clearly reasonable to choose the aspect estimate as $\hat{\varphi} \approx \varphi_6$.

We have quantified this idea by using the Maximum Likelihood Estimate (MLE) of aspect, that is, choosing $\hat{\varphi}$ as that value of φ which maximizes $L_i(Y; \varphi) = p(Y; \varphi | H_i)$ for a given value of Y . Strictly speaking, MLE calculation requires solving the equation [7]

$$\frac{\partial}{\partial \varphi} \left[\ln p(Y; \varphi | H_i) \right] = \frac{\partial}{\partial \varphi} \left[\ln p(Y; \varphi) H_i \right] \frac{\partial \sigma}{\partial \varphi} = 0$$

contain no explicit angular measurement and provide constraints on the aspect of the object. The aspect of the object is the angle between the line of sight and the normal to the object's surface.

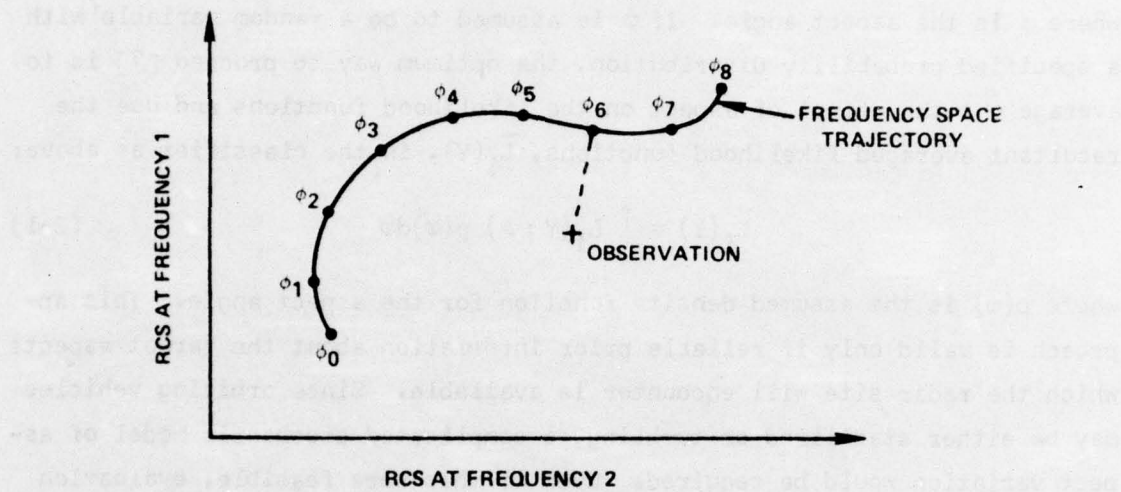


FIG. 6 The Geometry of Aspect Estimation

direction of a random vector measured on successive frequency bands. The angle between the observation vector and the frequency space trajectory is used as an aspect estimate. The aspect estimation is carried out with a linear programming technique. The observation vector is defined as the vector from the origin to the point of intersection of the frequency space trajectory and the observation vector. The aspect estimate is the angle between the observation vector and the frequency space trajectory.

where σ is the RCS of target i . This equation is, in general, too complicated for efficient exact solution so the aspect estimation is done by evaluating the likelihood function over a sufficiently fine grid of angles and choosing the aspect corresponding to the largest likelihood. If there are M targets in the library, there will be M aspect estimates, $\hat{\phi}^{(1)}, \hat{\phi}^{(2)}, \dots, \hat{\phi}^{(M)}$.

The classifier then operates by choosing the largest of

$$L_i(Y | \hat{\phi}^{(i)}) = p(Y; \hat{\phi}^{(i)} | H_i)$$

$i = 1, 2, \dots, M$. The superscript on the aspect variable is a reminder that the aspect estimate depends on which target is assumed to be present.

3.6 THE GENERALIZED LIKELIHOOD CLASSIFIER FOR A SINGLE LOOK

Figure 7 is a block diagram showing the major steps in the classifier algorithm. The processing is carried out in M parallel channels, one for each of the M targets in the signature library. The signature library or Frequency Space Trajectory (FST) file contains stored values of the RCS of each of the M targets as a function of frequency (and polarization) as well as aspect.

3.7 CLASSIFIER STRUCTURE FOR MULTIPLE OBSERVATIONS

The previous sections considered processing a single radar measurement (one pulse or the average of several pulses) of target RCS. If two looks at the target (Y_1 at time t_1 and Y_2 at time t_2) are available for processing, we could average to obtain $Y = (Y_1 + Y_2)/2$ and proceed as before. This approach is acceptable if the target has not changed aspect between observations but if the aspect has changed, the apparent target signature will be smeared and Y may be a poor representation of the true RCS.

If the target is changing aspect, we can appeal to the likelihood functions $p(Y_1, Y_2; \phi_1, \phi_2 | H_i)$ which describe the joint probability distributions of the two multifrequency observations of RCS under each hypo-

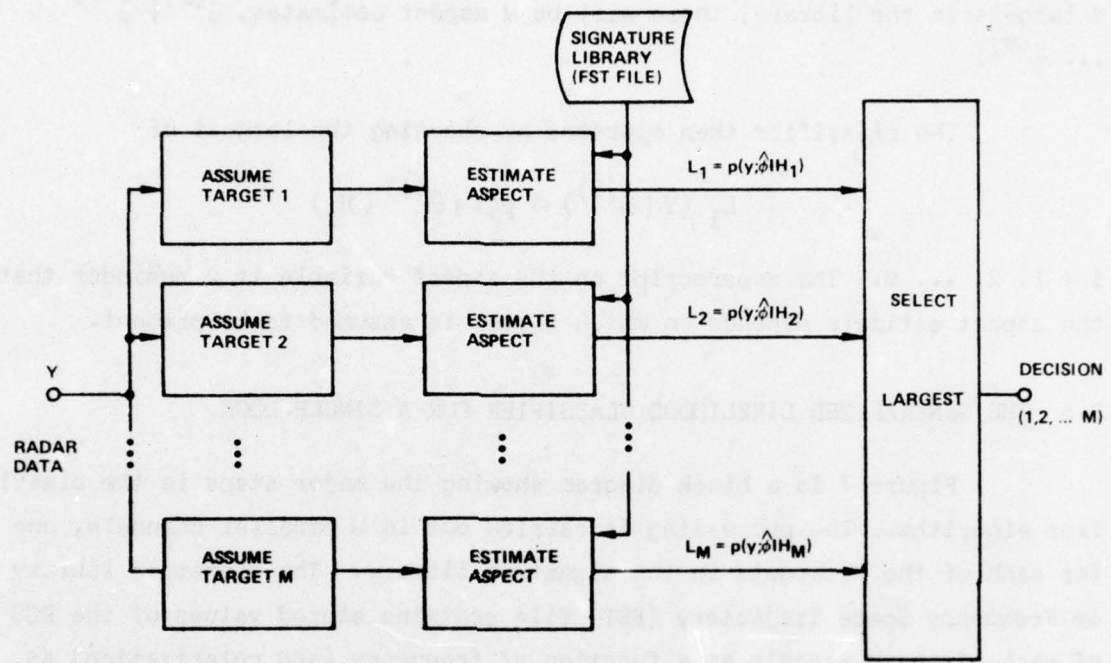


FIG. 7 The Generalized Likelihood Classifier for a Single Look

thesis. The observations Y_1 and Y_2 are random due to antenna noise and receiver thermal noise so that they are statistically independent and

$$p(Y_1, Y_2; \varphi_1, \varphi_2 | H_i) = p(Y_1; \varphi_1 | H_i) p(Y_2; \varphi_2 | H_i).$$

Using the maximum likelihood estimates of aspect, the generalized likelihood functions are

$$L_i(Y_1, Y_2) = p(Y_1; \hat{\varphi}_1^{(i)} | H_i) p(Y_2; \hat{\varphi}_2^{(i)} | H_i)$$

where

$$\hat{\varphi}_j^{(i)} = (\text{MLE of aspect given } Y_j \text{ assuming target } i \text{ is present}) \quad (3-2)$$

Note that the two-look generalized likelihood function is the product of two single-look generalized likelihood functions which are calculated as in Section 3.5 and shown in Figure 7. This idea clearly extends to any number of observations. If Y_1, Y_2, \dots, Y_N are a time sequence of multifrequency radar measurements of target RCS, the generalized likelihood functions are

$$L_i(Y_1, Y_2, \dots, Y_N) = \prod_{n=1}^N p(Y_n; \hat{\varphi}_n^{(i)} | H_i)$$

which indicates that the basic "building block" of the multi-observation processor is the single observation algorithm described in Section 3.5. The multiple observation classifier operates by evaluating the L_i for the M targets and selecting the target corresponding to the largest L_i .

Before giving the explicit configuration of the classifier, we note that the N -fold product of the single observation probability densities can be reduced to a summation by using the logarithm of the likelihood functions. There is no loss in classifier performance by doing this because likelihood functions (probability densities) are non-negative and the fact that $\ln L_i > \ln L_j$ implies that $L_i > L_j$. The classifier for N observations computes the M log-likelihood functions

$$s_i(Y_1, Y_2, \dots, Y_N) = \sum_{n=1}^N \ln p(Y_n; \hat{\varphi}_n^{(i)} | H_i) \quad (3-3)$$

$i = 1, 2, \dots, M$ and chooses the target corresponding to the largest of the S_i . A block diagram of this processor is shown in Figure 8. It has the same basic structure (M parallel channels) as the single-look processor. The only change is the addition of an accumulator between the aspect estimator and the comparator.

3.8 OPTIMALITY OF THE CLASSIFIER

The results of statistical decision theory [7] show that, given the prior distribution of target aspect, the decision rule using the likelihood functions given by equation (3-1) provides the optimum classifier in the sense of minimum error probability. Since we were unwilling to arbitrarily assume a prior distribution for aspect we have used the generalized likelihood (aspect estimation) approach. There are, unfortunately, no theorems relating to the optimality of this approach. It is however a well accepted technique for composite hypothesis testing [7] and can be used to synthesize many of the classical techniques of mathematical statistics (such as analysis of variance [8] and signal detection [7, 9]). The final assessment of its efficacy must be based on its performance. This subject is discussed in Section 4.

The optimality of any method depends on the assumed model. If the model is not a valid description of the physical world, the optimality of a technique is of little importance. The study of optimal classifiers can, however, lead to important concepts concerning the basic structure of target classification processors. In this context, the importance of the probability distribution (likelihood function) of the radar observations cannot be overemphasized.

3.9 SUMMARY

Classifier design is basically the selection of a measure of the closeness between the observed radar data and the signatures stored in the frequency space trajectory file. By appealing to the powerful concepts of statistical hypothesis testing we have synthesized this proximity measure

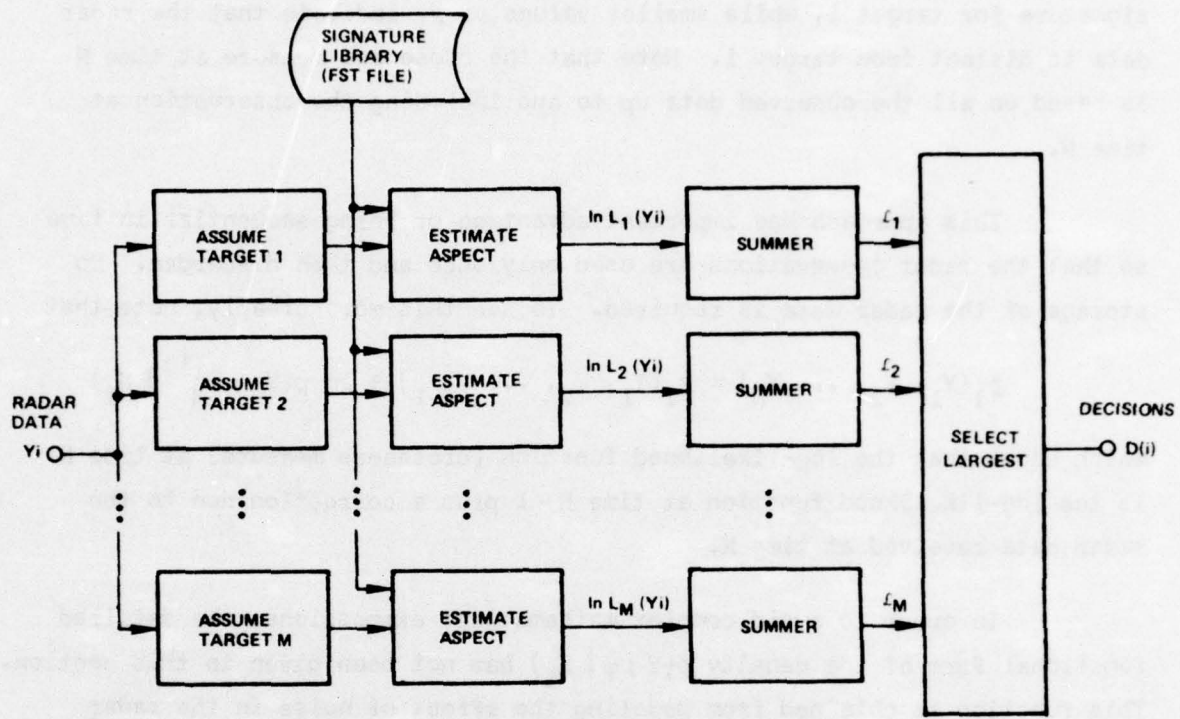


FIG. 8 The Generalized Likelihood Classifier for Multiple Observations

from the log likelihood functions, \mathfrak{L}_i , which are basically the joint probability density functions of the radar measurements of RCS. Larger values of \mathfrak{L}_i indicate that the radar data Y_1, Y_2, \dots, Y_N is close to the stored signature for target i , while smaller values of \mathfrak{L}_i indicate that the radar data is distant from target i . Note that the closeness measure at time N is based on all the observed data up to and including the observation at time N .

This approach has important advantage of being sequential in time so that the radar observations are used only once and then discarded. No storage of the radar data is required. To see this more clearly, note that

$$\mathfrak{L}_i(Y_1, Y_2, \dots, Y_N) = \mathfrak{L}_i(Y_1, Y_2, \dots, Y_{N-1}) + \ln p(Y_N; \hat{\varphi}_N^{(i)} | H_i)$$

which shows that the log-likelihood function (closeness measure) at time N is the log-likelihood function at time $N-1$ plus a correction due to the radar data received at time N .

In order to avoid complex mathematical expressions, the detailed functional form of the density $p(Y; \varphi | H_i)$ has not been given in this section. This function is obtained from modeling the effect of noise in the radar receiver and is derived in an Appendix.

SECTION 4

TARGET CLASSIFICATION PERFORMANCE

This section describes the results of Monte Carlo simulations of realistic Satellite Object Identification (SOI) scenarios. Particular attention is given to determining how soon after target acquisition the classification technique can reliably determine the target shape. Both stabilized and tumbling vehicles are considered.

4.1 HORIZON STABILIZED VEHICLES

The horizon stabilized case considered here assumes that the longitudinal axis of the target is oriented along its velocity vector. If the vehicle has a circular orbit, its longitudinal axis is always parallel to the earth's surface. An analogy is a bus driving on a great circle road around the earth.

4.1.1 Orbital Geometry and Aspect Variation

Investigation of all possible orbits was well outside the scope of this study. For simplicity and because most space vehicles have orbits with small eccentricity [6] a circular orbit was assumed. The orbital motion software written for this study simulates the flight of a target in a circular orbit about the earth which rotates at 15 degrees per hour. The important outputs of this program are target elevation, range, and aspect angle with respect to the radar site. Figure 9 shows the geometrical parameters describing this orbit [10, 11]. The radar site is assumed to be at Kwajalein: its location has been exaggerated in Figure 9.

The specific orbit considered here has inclination 98° (nearly polar), altitude 740 kilometers, and period 99.6 minutes. The orbital motion was then completely specified by assuming an initial (time equal to zero) ground track position on the equator at the Greenwich meridian. Under these conditions, the satellite will not be visible to the radars until about 40

a = ORBIT RADIUS
 i = ORBIT INCLINATION
 Ω = LONGITUDE OF ASCENDING NODE

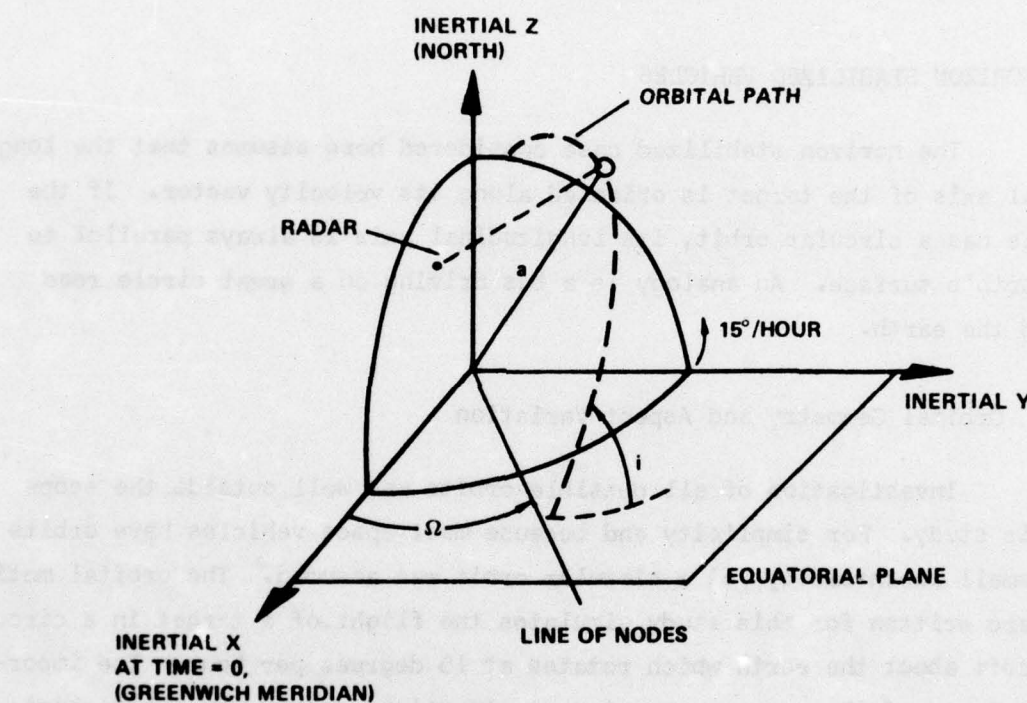


FIG. 9 Parameters for a Circular Orbit

minutes later. This first pass which lasts about 14 minutes was used to test the classification method.

The range and aspect for a horizon stable target as a function of time from satellite rise is shown in Figure 10. The range varies between 3118 and 775 km. The range and elevation at the Point of Closest Approach (PCA) are 775 km and 72 degrees. The aspect increases monotonically from 28 to 154 degrees and broadside aspect (90 degrees) occurs at PCA where the most rapid aspect change also occurs.

4.1.2 Monte-Carlo Results for Correct Classification Rate

Time varying noisy radar cross section (scaled received signal power) measurements were simulated using the range and aspect variations shown in Figure 10 and the probability distributions developed in Appendix 10.2. Figures 11 and 12 are an example of the simulated radar data at VHF and UHF respectively for the two non-spherical targets. Each point on the plots represents a 10 pulse estimate of RCS as seen by the ALTAIR radar. These curves are analogous to the RCS* strip charts sometimes used to estimate the shape and size of space objects by means estimated target motion (aspect variation) and studying the structure of the lobes or speculars [12].

The large amplitude random fluctuations in the RCS measurements during the early and late portions of the pass are due to the low signal to noise ratios which occurs at long range. Near PCA the target is much closer and displays the larger broadside RCS so that the effect of the noise is almost negligible.

The classifier was tested by driving it with time samples of random data similar to that in Figures 11 and 12. One hundred passes of each of the three targets (using independent noise on each pass) were processed to obtain a Monte-Carlo estimate of the probability of correct classification,

* Figures 11 and 12 are not really plots of apparent RCS in dB, but are plots of $10 \log_{10} (1 + 10 \text{ RCS}) - 10$ so that the lowest value will be -10. This presentation is used to better display the lobe structure by suppressing large negative RCS values. The correspondence to RCS in dB is very close.

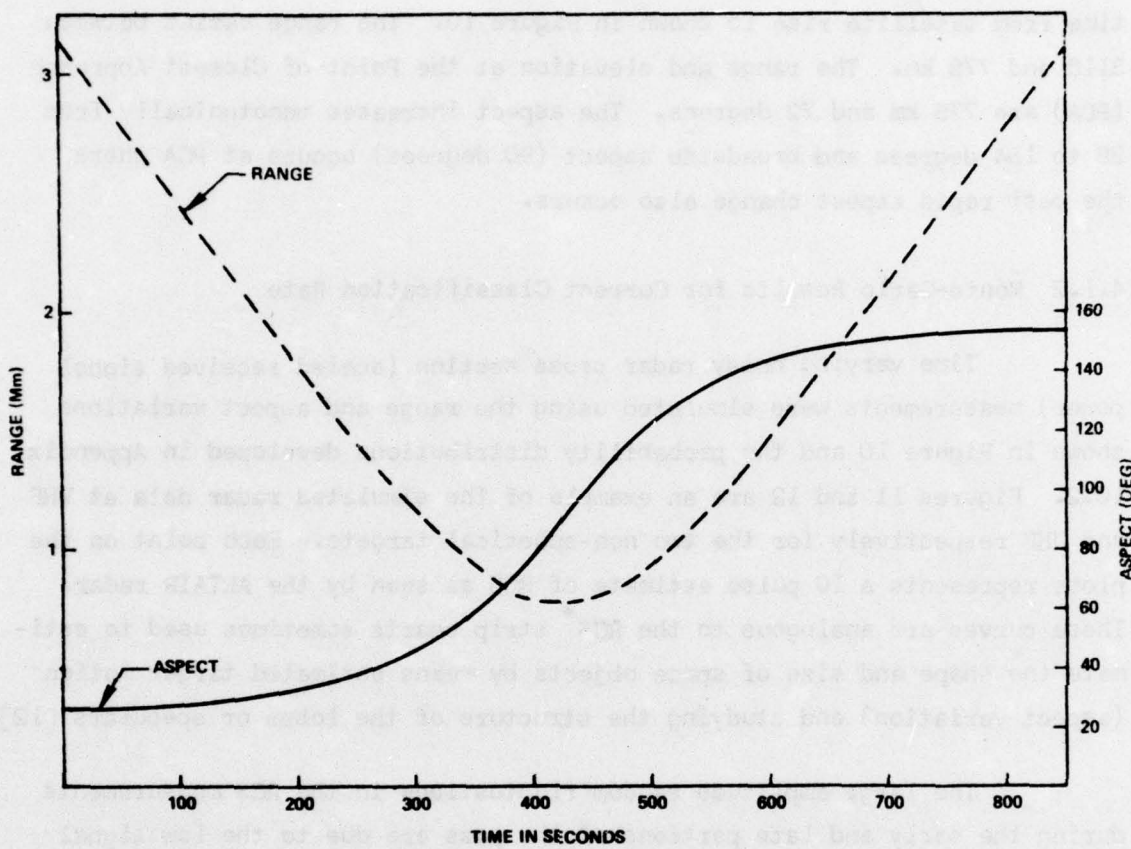


FIG. 10 Range and Aspect Variation During Pass of Horizon Stabilized Vehicle

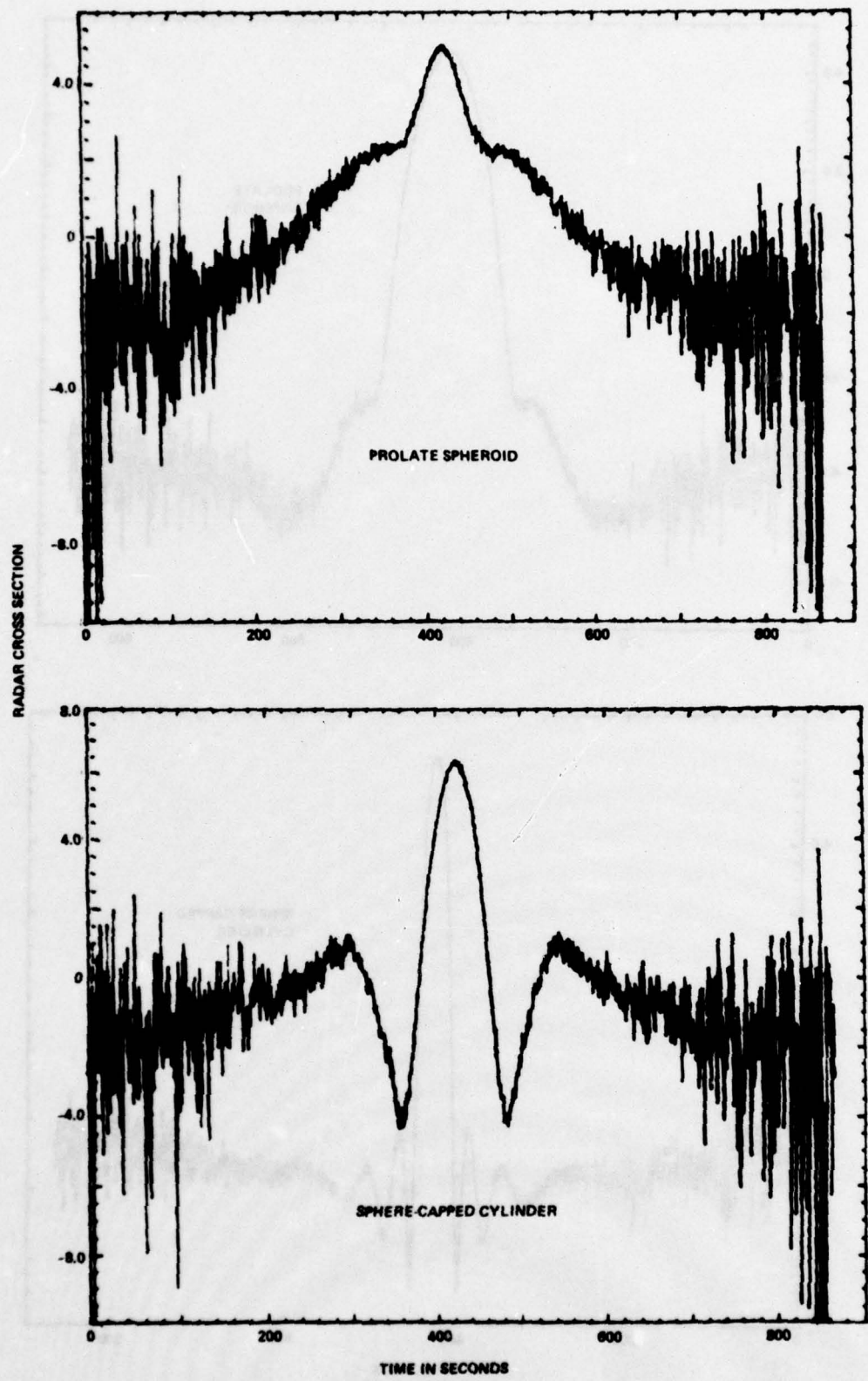


FIG. 11 Apparent Noisy RCS at 155.5 MHz (ALTAIR - VHF)

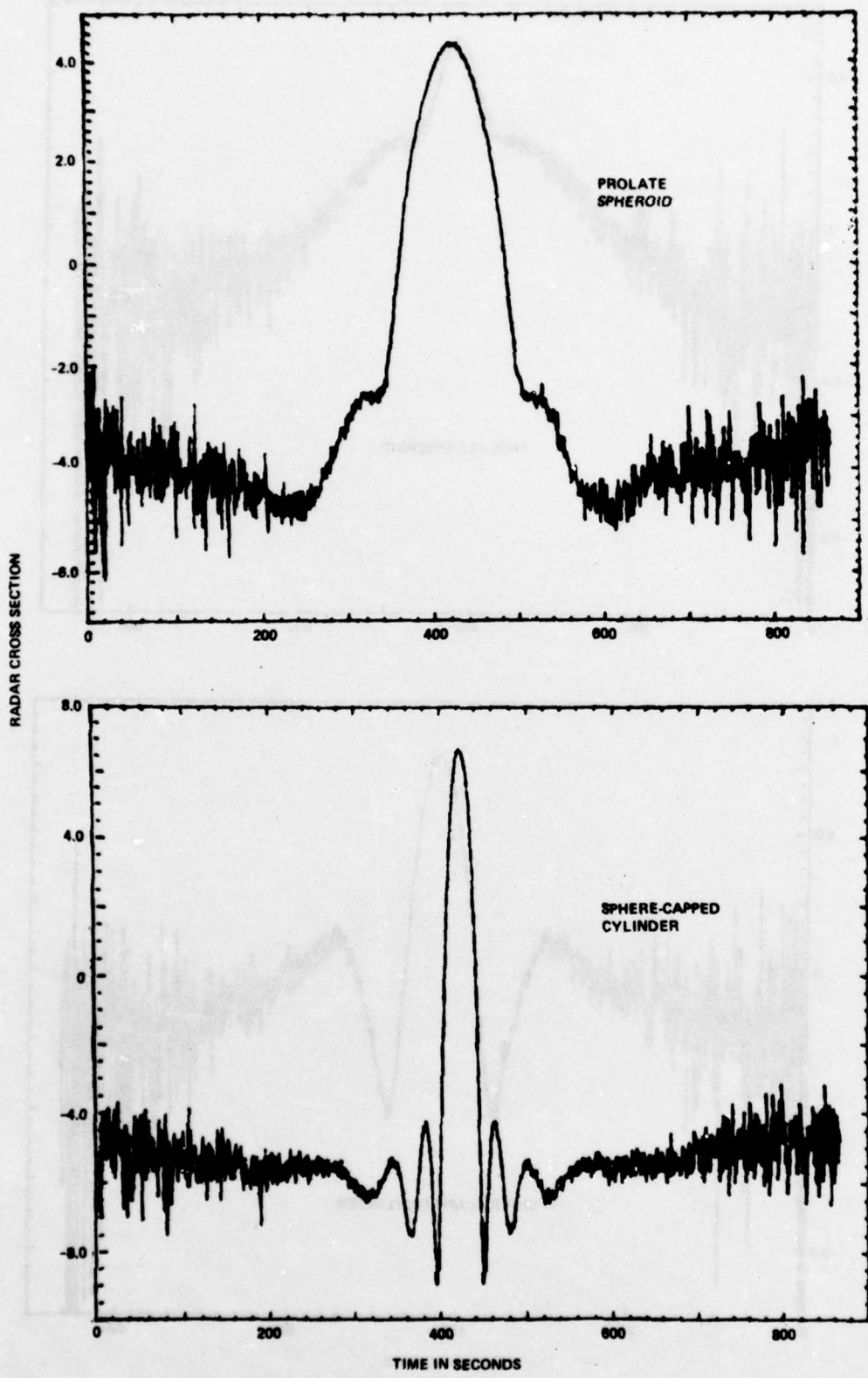


FIG. 12 Apparent Noisy RCS at 415 MHz (ALTAIR - UHF)

\hat{P}_c , defined by

$$\hat{P}_c = \left[\hat{P}_c(S) + \hat{P}_c(PS) + \hat{P}_c(SCC) \right] / 3$$

where

$\hat{P}_c(S) = \text{number of trials sphere was correctly classified} / 100$

$\hat{P}_c(PS) = \text{number of trials prolate spheroid was correctly classified} / 100$

$\hat{P}_c(SCC) = \text{number of trials sphere-capped cylinder was correctly classified} / 100$

Since the classifier makes a new decision after every observation during a pass, these probabilities can be viewed as functions of time or the number of observations since the beginning of the pass. Figure 13 is a plot of \hat{P}_c versus time for the case where the radars make one ten-pulse observation every 28 seconds -- a total of 31 observations of RCS during the pass. The results for four different selections of multifrequency operation are shown: using only VHF and UHF (ALTAIR), using only L and S bands (TRADEX), and using all frequencies (ALTAIR and TRADEX). In the last case, perfect classification performance is obtained after only eleven observations. This occurs about 280 seconds after satellite rise, which is well before any significant evidence of lobing or speculars appears in the data (see Figures 11 and 12). This result demonstrates the rapid classification capability of the generalized likelihood, frequency space trajectory method.

Figure 13 also indicates that the method is not as effective when only the two lower frequencies (ALTAIR) are used. The probability of correct classification at the earlier times is reduced and the time required for perfect classification is increased by 28 seconds (one additional observation). Note that this time is still much less than would be required by analysts who use the lobe shapes.

If only the high frequencies are used, perfect classification does not occur until PCA. This is due in part to the closeness of the sphere and the prolate spheroid at these frequencies (see Figure 3) and possibly

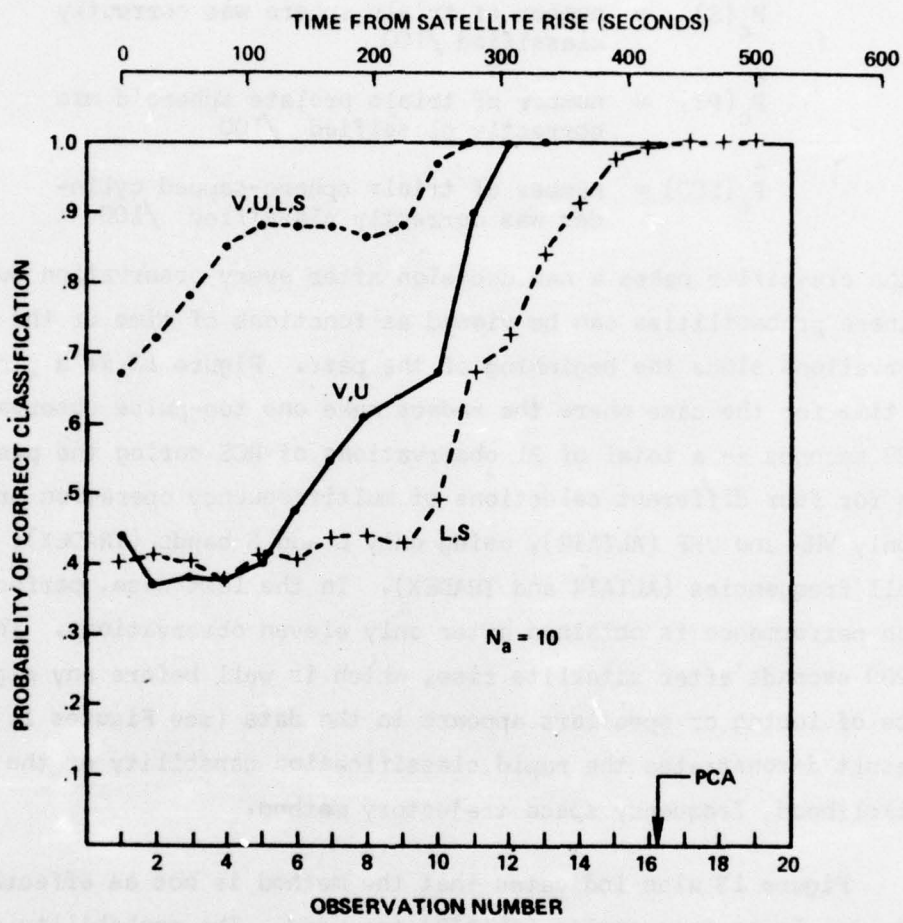


FIG. 13 Classification Performance for Horizon Stabilized Targets

also due to the coarse aspect increment in the frequency space trajectory file. In any case, the addition of the higher frequency information to the lower frequency data is seen to significantly improve the classification performance.

Figure 14 shows the classification performance obtained when observations based on the average of 100 pulses are used. As is expected, perfect classification occurs earlier than when 10 pulse averages are used although the differences slight for the VHF/UHF case. An examination of Figure 2 provides the explanation for this. Note that the prolate spheroid and sphere-capped cylinder frequency space trajectories are nearly identical for aspects in the region 25 to 40 degrees which, as shown in Figure 10, is the range of aspects seen in the early portions of the pass. It is therefore not surprising that reliable classification at VHF/UHF cannot occur until the target aspect exceeds 40 degrees. Although increased pulse averaging appears to improve performance, there is a limit to the number of pulses which can be averaged imposed by the aspect variation of the vehicle. For this reason we have emphasized the ten-pulse average case.

4.1.3 Aspect Estimation Performance

As discussed in Section 3, aspect estimation is automatically accomplished as a fundamental part of the target classification method. Figure 15 shows an example of the maximum likelihood aspect estimates provided when all four frequencies (ALTAIR and TRADEX) are used and the prolate spheroid is in a horizon stable orbit. The circles indicate the value of the aspect estimated under the hypotheses that the prolate spheroid is present, that is, the circles are the estimates produced in the classifier channel (see Figure 8) which corresponds to the prolate spheroid. These estimates cluster very closely about the true aspect represented by the solid line. At long range (low signal to noise ratio) the error is greatest as expected.

The fluctuating curve indicated by the crosses is the aspect estimate under the incorrect hypothesis that the sphere-capped cylinder is present. The erratic behavior of this curve is, for stabilized targets, indicative

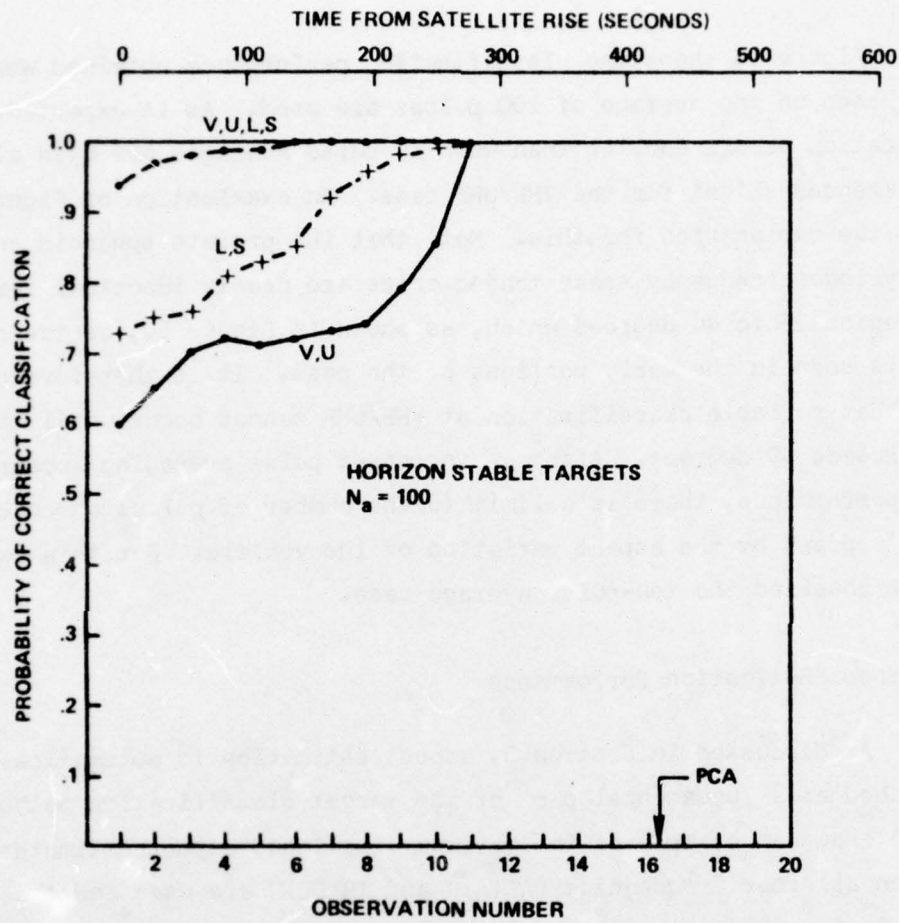


FIG. 14 Classification Performance, $N_a = 100$

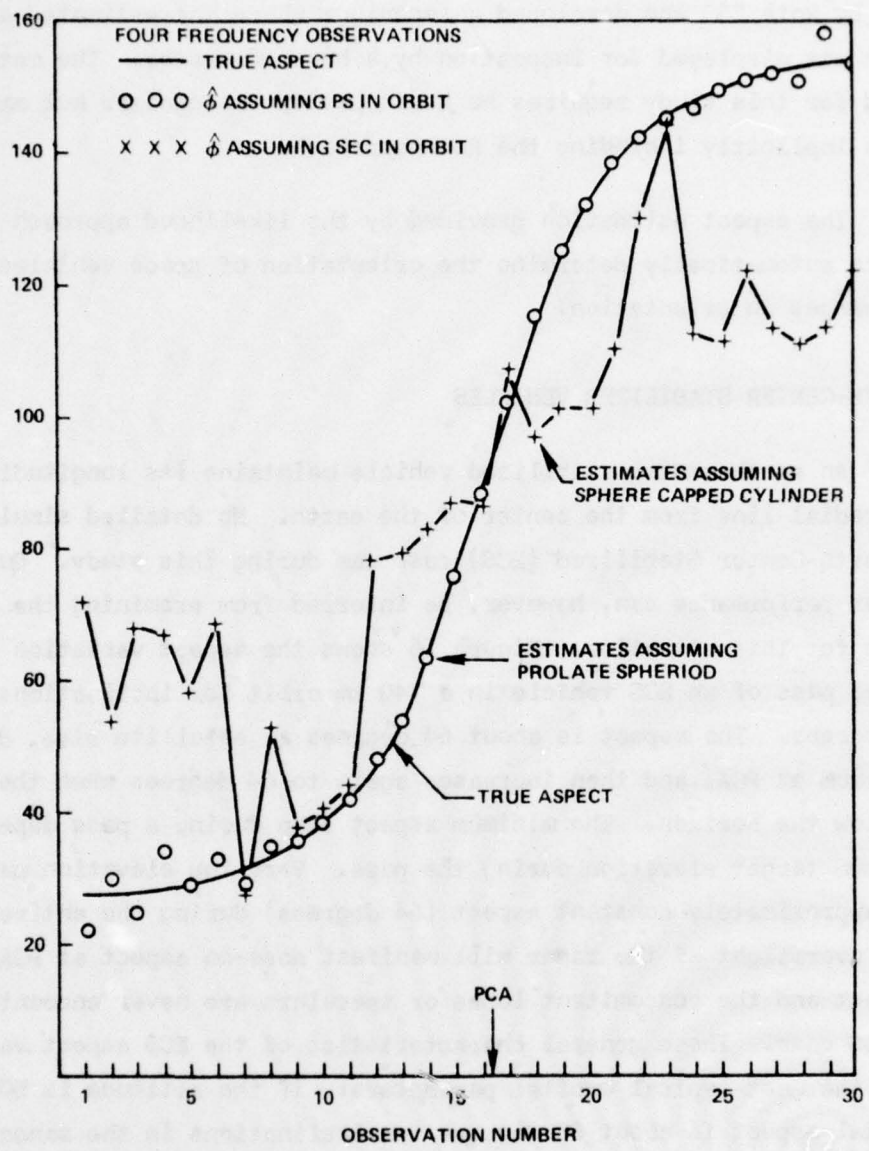


FIG. 15 Estimated Aspect for Orbiting Prolate Spheroid

of an incorrect target shape hypothesis. This approach to classification was used by Roth [3] who developed a technique where the estimated aspect variation was displayed for inspection by a human operator. The method developed for this study requires no human pattern recognizer but may be viewed as implicitly including the Roth approach.

The aspect estimation provided by the likelihood approach could be used to automatically determine the orientation of space vehicles or to detect changes in orientation.

4.2 EARTH-CENTER STABILIZED VEHICLES

An earth-center stabilized vehicle maintains its longitudinal axis along a radial line from the center of the earth. No detailed simulation of the Earth-Center Stabilized (ECS) case was during this study. Qualitative classifier performance can, however, be inferred from examining the aspect variation for this situation. Figure 16 shows the aspect variation during a selected pass of an ECS vehicle in a 740 km orbit for inclinations of 30 and 90 degrees. The aspect is about 64 degrees at satellite rise, decreases to a minimum at PCA, and then increases again to 64 degrees when the target moves below the horizon. The minimum aspect seen during a pass depends on the maximum target elevation during the pass. Very low elevation passes have an approximately constant aspect (64 degrees) during the entire pass. A direct overflight of the radar will manifest nose-on aspect at PCA. Broadside aspect and the concomitant lobes or speculars are never encountered in the ECS case. These general characteristics of the ECS aspect variation apply to the most typical orbital parameters: if the altitude is 500 km, the initial aspect is about 68 degrees for inclinations in the range 30 to 90 degrees.

The frequency space trajectories in Figure 2 and the results for the horizon stable case indicate that ECS targets can be rapidly classified by the method developed in this study. The initial aspect being roughly 60 degrees implies a large difference (several dB) between the multifrequency RCS of the different targets. Even allowing time for target acquisi-

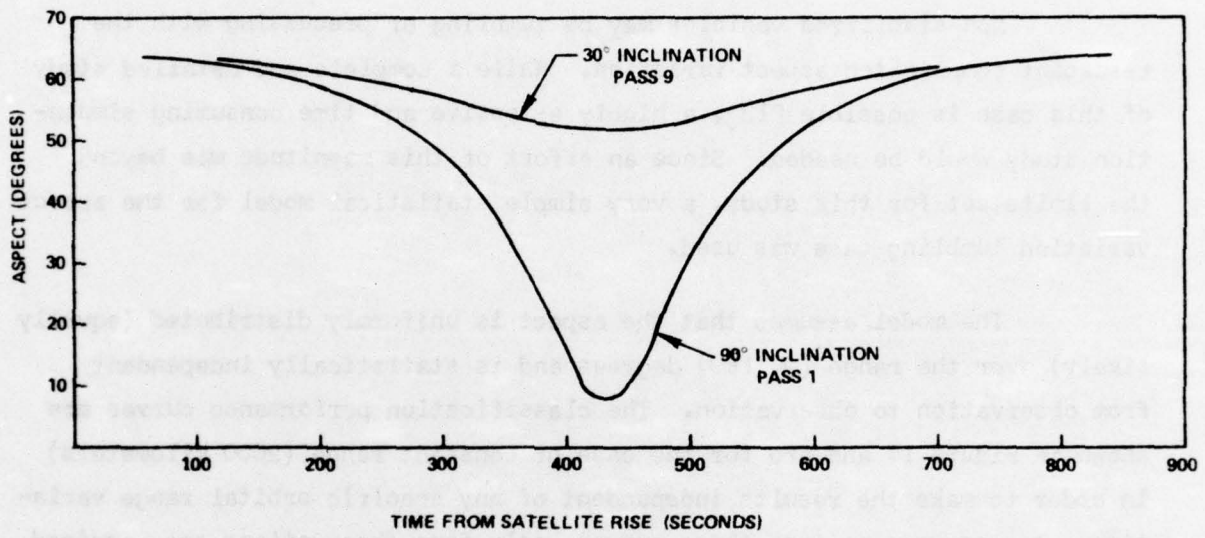


FIG. 16 Aspect Variation for ECS Vehicles

tion (track data may not begin until the smaller aspects) the reduced range increases the signal to noise ratio implying good classification performance. In contrast to the horizon stabilized case, where similar target RCS and long range occurred simultaneously, for the ECS situation these factors tend to cancel.

4.3 TUMBLING VEHICLES

Non-stabilized vehicles may be tumbling or precessing with the resultant complicated aspect variation. While a complete and detailed study of this case is possible [13], a highly extensive and time consuming simulation study would be needed. Since an effort of this magnitude was beyond the limits set for this study, a very simple statistical model for the aspect variation tumbling case was used.

The model assumes that the aspect is uniformly distributed (equally likely) over the range (0, 180) degrees and is statistically independent from observation to observation. The classification performance curves are shown in Figure 17 and are for the case of constant range (2000 kilometers) in order to make the results independent of any specific orbital range variation. As can be seen from these curves, only four observations are required for perfect classification when all four frequencies are used. Measurements at the two lower frequencies (VHF/UHF) require about 13 observations.

Reliable classification is never achieved when only the two high frequencies (L and S bands) are used. There are two major factors contributing to this result. The most important factor is the proximity between the sphere and prolate spheroid RCS at these frequencies (see Figure 3). The second factor is that the signal to noise ratio does not improve with time. When the sphere is orbiting, the RCS observations will be randomly distributed about the true sphere RCS. Since the prolate spheroid RCS lies on a line very near the true sphere RCS, the observations have a greater probability of falling closer to the prolate spheroid (there are many possible vector values of RCS for the prolate spheroid, but only one for the sphere). For this reason the sphere is almost always classified as the prolate

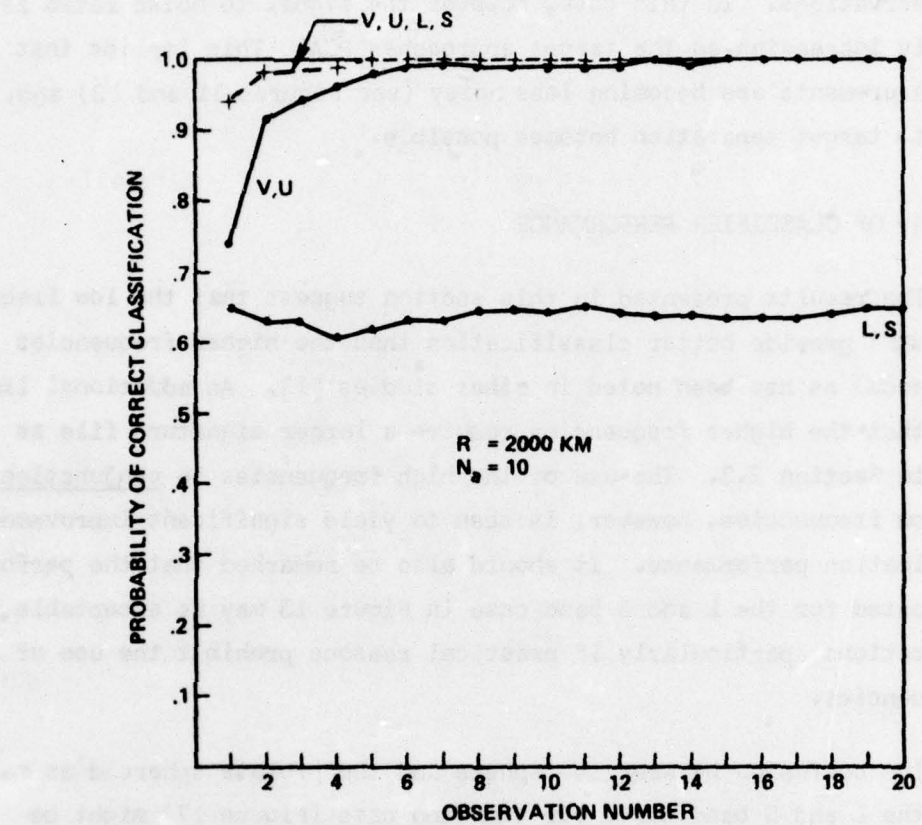


FIG. 17 Classification Performance: Tumbling Targets

spheroid.

Note that the same phenomenon occurred in the case of orbiting horizon stable targets. As can be seen from Figure 13, the classification performance at the high frequencies remained relatively poor for the first several observations. In this case, however the signal to noise ratio is continuously increasing as the target approaches PCA. This implies that the RCS measurements are becoming less noisy (see Figures 11 and 12) and, as a result, target separation becomes possible.

4.4 SUMMARY OF CLASSIFIER PERFORMANCE

The results presented in this section suggest that the low frequencies (VHF/UHF) provide better classification than the higher frequencies (L and S bands) as has been noted in other studies [1]. An additional limitation is that the higher frequencies require a larger signature file as discussed in Section 2.3. The use of the high frequencies in conjunction with the low frequencies, however, is seen to yield significant improvements in classification performance. It should also be remarked that the performance indicated for the L and S band case in Figure 13 may be acceptable for some applications, particularly if practical reasons prohibit the use of lower frequencies.

The confusion between the sphere and the prolate spheroid as manifested by the L and S band curve for tumbling case (Figure 17) might be regarded as a weakness of the classifier algorithm, especially in view of the large difference between the frequency space-trajectories for these two targets at most aspects. It might reasonably be stated that if the RCS values do not change with time (other than any noise-produced variations) the target must be a sphere and the classifier should be able to recognize this. This argument is, however, based on the implicit prior assumption that all targets significantly change aspect during observation by the radar site. The classifier is unwilling to make this assumption and, as a result, has difficulty distinguishing between the sphere and the prolate spheroid (at the higher frequencies) because they have almost identical RCS when

the prolate spheroid is at a certain aspect. The important point is that, in the absence of prior information about target aspect, the radar data from the sphere and the prolate spheroid at this aspect are not sufficiently different to allow reliable classification.

A related phenomenon occurs when a higher observation rate is used for the classification of horizon stabilized targets. For example, our results show increasing the observation rate from one every 28 seconds to one every four seconds does not greatly change the classification performance. This may seem surprising, because the classifier could average blocks of the observations at this higher observation rate to yield lower variance data at the 28 second interval from which one would expect improved performance. As pointed out previously, however, observation averaging is useful only when the target is not changing aspect: if otherwise, the target signature will be smeared or blurred resulting in very poor performance. In order for the classifier to take advantage of observation smoothing, it must have good prior information about the statistics of target aspect variation. The classifier developed here is based on a conservative approach which enables classifying targets with any realistic dynamic motion. Our approach represents a good tradeoff between the desire for a high performance classifier for a specific aspect variation and the desire for a classifier which will, at the same time, be applicable to any conceivable aspect variation.

If valid, quantitative, prior statistical information concerning the aspect variation of targets were available, it could be used to develop an improved classifier following the guidelines of statistical decision theory as discussed in Section 3.4. Such an effort would be a logical follow-on to this study and could also include other effects such as random ionospheric scintillation [14] which has been neglected here.

SECTION 5

A DECISION CONFIDENCE MEASURE

It must be recognized that situations will occur when any classifier cannot reliably decide which target is present. In this event, it is important for the classification method to be able to notify the output user that low confidence is associated with its current decision. The development of a decision confidence measure is discussed in this section.

5.1 DESCRIPTION OF THE CONFIDENCE MEASURE

The basic outputs of the classification processor are the logarithms of the M generalized likelihood functions as illustrated in Figure 8 and described in Section 3.7. These outputs are defined by

L_1 = log likelihood assuming target 1 is present,

L_2 = log likelihood assuming target 2 is present,

•

•

•

L_M = log likelihood assuming target M is present.

These outputs accumulate with time as the satellite is viewed by the radar site, but after each observation the classifier then finds the largest of these numbers, L_k for example, and decides that target k is present. Note that all these numbers are functions of the noisy radar observations and are themselves random variables.

It may occur that one of the other log likelihood values, say L_j , is only slightly smaller than L_k . In this case, there is not a clear choice as to whether target k or j is present, but the classifier will decide target k and it is desirable for the classifier to recognize that its decision is not clear-cut.

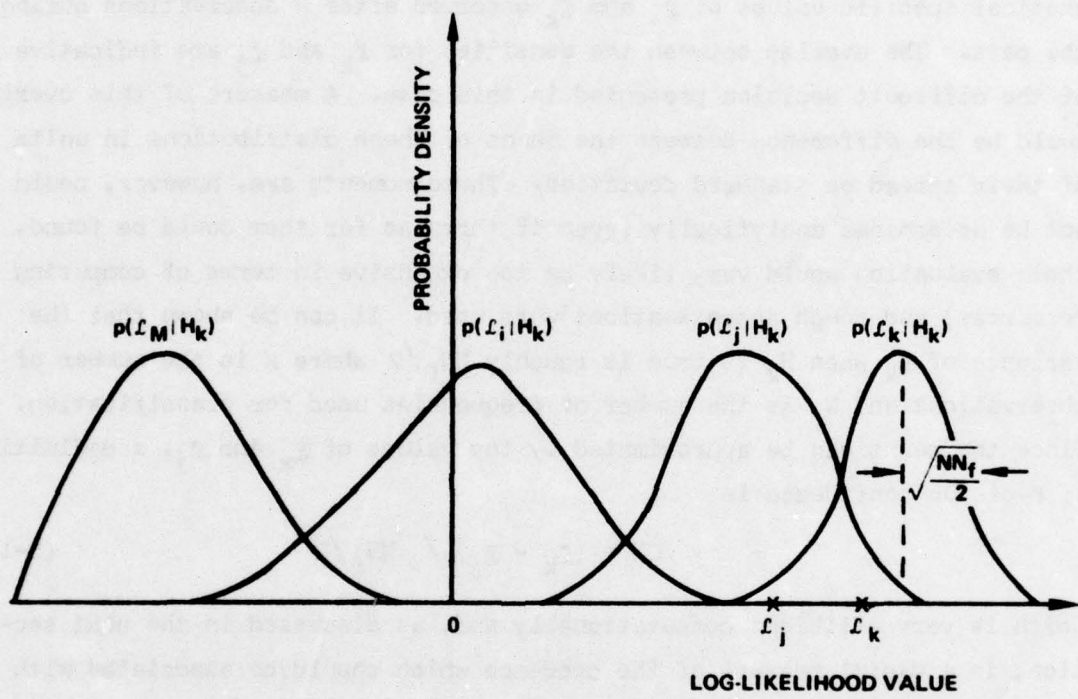


FIG. 18 Illustrating the Probability Densities of the Classifier Outputs after N Observations When H_k is True

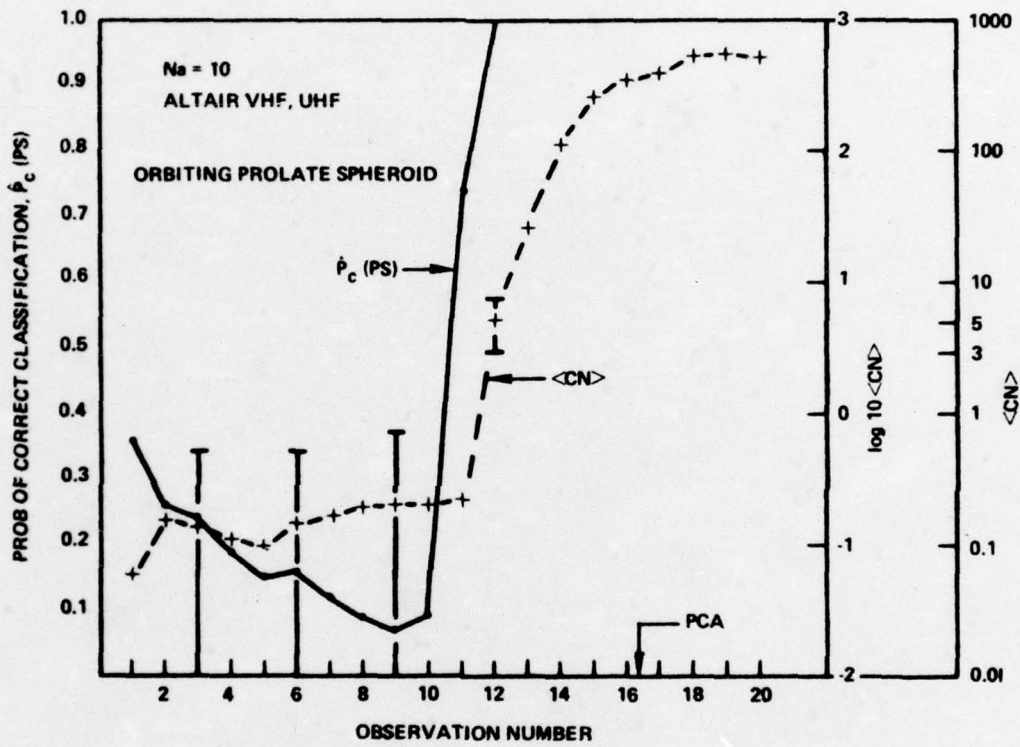
Since the numbers ξ_k and ξ_j are random variables, the quantification how clear-cut the decision is must be based on the probability distributions of ξ_k and ξ_j . These distributions are extremely complicated so an approximation is used. Figure 18 is a sketch illustrating the probability densities of the random variables $\xi_1, \xi_2, \dots, \xi_M$ when target k is being observed by the radar site. On the abscissa of this plot are shown the hypothetical specific values of ξ_j and ξ_k observed after N observations during the pass. The overlap between the densities for ξ_k and ξ_j are indicative of the difficult decision presented in this case. A measure of this overlap would be the difference between the means of these distributions in units of their spread or standard deviation. These moments are, however, could not be determined analytically (even if formulas for them could be found, their evaluation would very likely be too expensive in terms of computing resources) and rough approximations were used. It can be shown that the variance of ξ_k when H_k is true is roughly $NN_f/2$ where N is the number of observations and N_f is the number of frequencies used for classification. Since the means can be approximated by the values of ξ_k and ξ_j , a definition of decision confidence is

$$CN = (\xi_k - \xi_j) / \sqrt{NN_f/2} \quad (5-1)$$

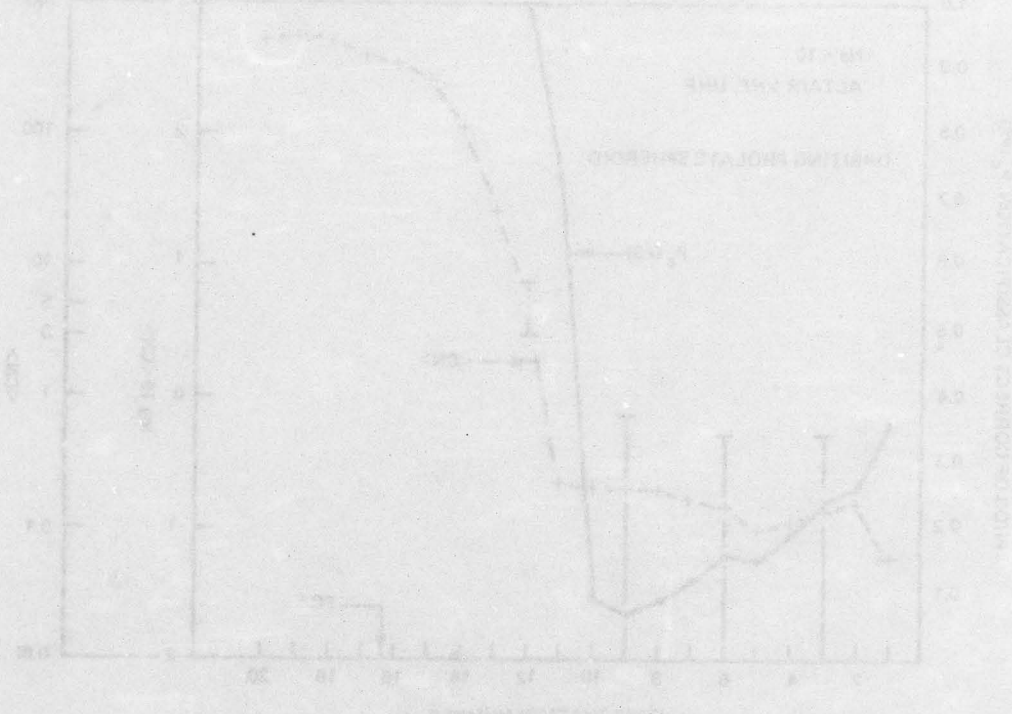
which is very efficient computationally and, as discussed in the next section, is a useful measure of the credence which should be associated with the classifier decisions.

5.2 PERFORMANCE OF THE DECISION CONFIDENCE MEASURE

Figure 19 shows the correspondence between the probability of correctly classifying the horizon stabilized prolate spheroid and the average confidence number, $\langle CN \rangle$, for 100 Monte Carlo trials. The standard deviation of CN is indicated by the "error bars" about the $\langle CN \rangle$ curve. Note that when the confidence is low, the probability that the decision is correct is also low. This plot indicates that when the decision confidence exceeds 3, the associated decision is very reliable. As the target approaches PCA the confidence number becomes very large, requiring the logarithmic scale and indicating the large separation (in standard deviations) between the two



distributions as in equation (5-1). The confidence number could be used to make the earliest possible decisions depending on the desired probability of correct classification which could be specified based on operational requirements.



SECTION 6

REJECTION OF UNKNOWN TARGETS

The classifier will always make a decision about which target is present, even though the target being illuminated may be very different from any of the targets in the signature library. This decision could also be made with high confidence, CN, because the confidence number is a measure of the confusion between the targets which are actually in the library. It is therefore desirable that the classification system be able to recognize that the received radar data is not consistent with any of the stored library signatures.

6.1 DESCRIPTION OF THE REJECTION METHOD

This capability can be provided by again appealing to the probability distributions of the classifier outputs $\xi_1, \xi_2, \dots, \xi_M$. Suppose the classifier has decided that target k is present (that is ξ_k is the largest of the outputs). If this is in fact true, the observed value of ξ_k should lie close to the mean of the distribution of ξ_k under the hypothesis that target k is present. If target k is not present, the observed value of ξ_k will tend to be smaller by the definition of our likelihood closeness measure. The situation is sketched in Figure 20 where we show the probability density of ξ_k when H_k is true and a hypothetical observed value of ξ_k when some other (unknown) target is being illuminated. The greater the distance between ξ_k , the observed value, and the mean of the distribution of ξ_k when target k is really present, the less likely that target k is being observed. A probabilistic measure of this distance is

$$RCN = (E[\xi_k | H_k] - \xi_k) / \sqrt{NN_f/2} \quad (6-1)$$

where $E[\xi_k | H_k]$ is the mean of ξ_k when H_k is true and $NN_f/2$ is an approximation to the corresponding variance. Equation (6-1) is the basic definition of rejection confidence and is evaluated using an approximate formula for the mean. When RCN is small (or negative) the received radar data is close to target k . Large values of RCN indicate that the received data is

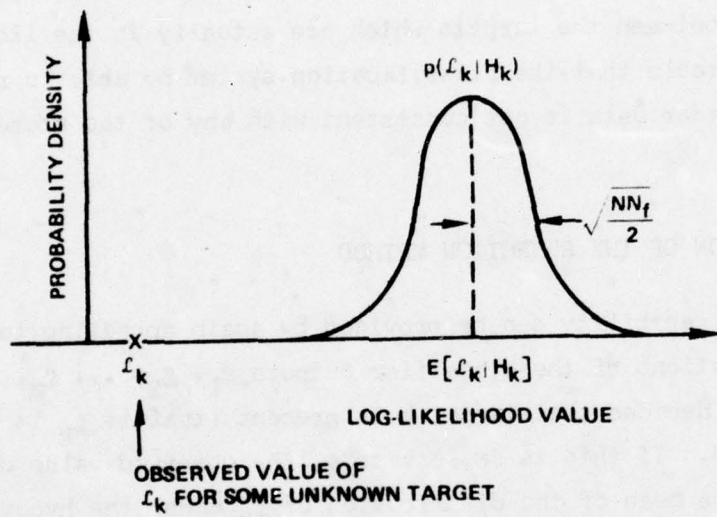


FIG. 20 Probability Considerations for the Reject Method

not representative of any of the targets in the signature library; that is, an unknown target is being illuminated.

6.2 TEST RESULTS FOR TARGET REJECTION

Ross [15] has developed geometrical diffraction theory formulas for the RCS of several bodies of revolution. Figure 21 shows the frequency space trajectories obtained with his method at VHF/UHF for a right circular cylinder* of length 3 meters and diameter 1 meter. The estimated mean (by Monte Carlo simulation) of the rejection confidence is shown in Figure 22. The three curves show the average of RCN as a function of the time from satellite-rise when the horizon stabilized right circular cylinder, the sphere-capped cylinder, and the sphere, respectively, move in orbit through the field of view of the radar site. Note that the rejection confidence measure behaves as desired: targets not in the library very quickly manifest a large RCN, while targets in the library have a small RCN. The prolate spheroid is not shown on this plot because it is very similar to the other two targets in the library.

Although the approximation to RCN is somewhat crude, the results indicate that it is an effective means of recognizing the presence of an unknown target. A better approximation could be developed but would be much more expensive in computer time.

*This cylinder response was used in the initial stages of the present study. Since it was already available, it has been used to test the rejection method. Note that, mathematically speaking, the study of classifier performance is the study of frequency space trajectories.

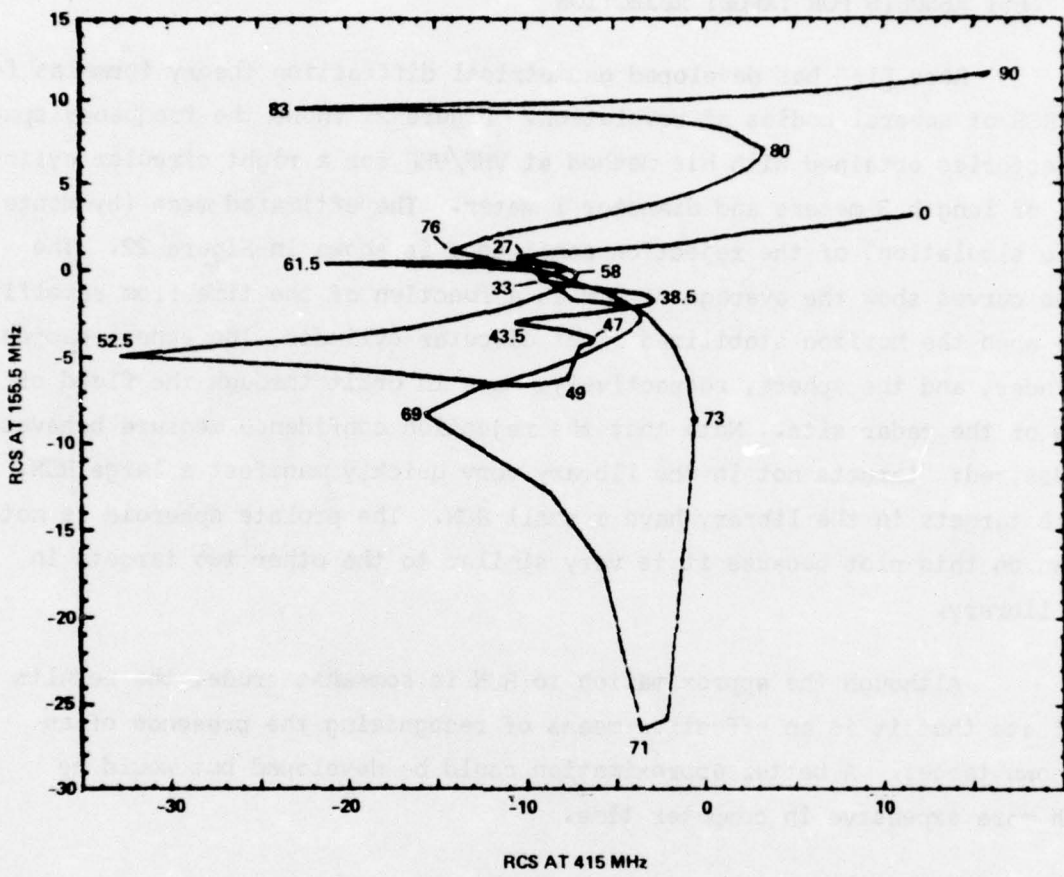


FIG. 21 Approximate Frequency Space Trajectories Right Circular Cylinder

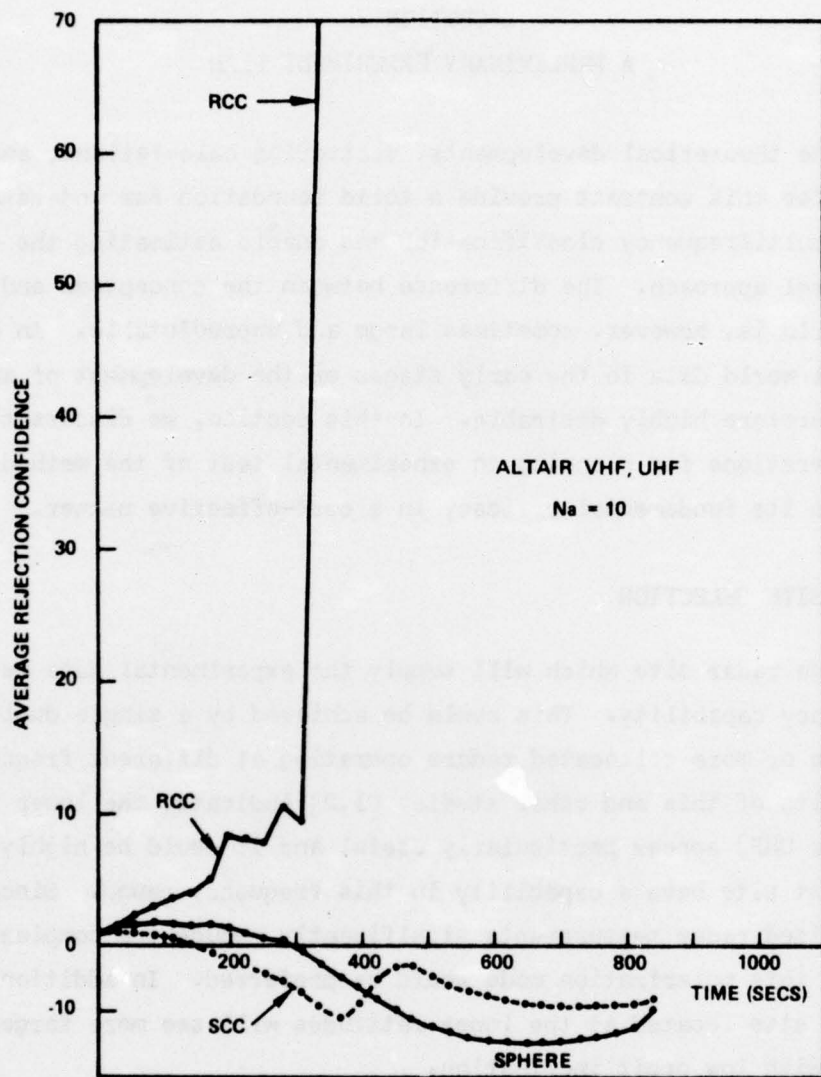


FIG. 22 Performance of Rejection Confidence Measure

SECTION 7
A PRELIMINARY EXPERIMENT PLAN

The theoretical developments, scattering calculations, and simulations done for this contract provide a solid foundation for understanding the problem of multifrequency classification and enable estimating the efficacy of the general approach. The difference between the conceptual and the real physical world is, however, sometimes large and unpredictable. An examination of real world data in the early stages of the development of any technique is therefore highly desirable. In this section, we discuss the important considerations for planning an experimental test of the method which will examine its fundamental efficacy in a cost-effective manner.

7.1 RADAR SITE SELECTION

The radar site which will supply the experimental data must have a multifrequency capability. This could be achieved by a single dual-frequency radar or two or more collocated radars operating at different frequencies. As the results of this and other studies [1,2] indicate, the lower frequencies (VHF or UHF) appear particularly useful and it would be highly desirable that the test site have a capability in this frequency range. Since circularly polarized radar measurements significantly reduce the complexity of the classifier, this polarization mode would be preferred. In addition, a high power radar site located at the lower latitudes will see more targets [6], even those with low orbit inclination.

It is also important that the collection of accurate data does not interfere with the normal operational requirements of the site. This suggests the selection of a radar installation where the multifrequency recording of accurate data from high-altitude, long range targets is a routine operation. All these considerations strongly indicate that data from the Pacific Range Electromagnetic Signature Study (PRESS) radars ALTAIR and TRADEX would very likely provide a cost effective and meaningful experimental test of the multifrequency object classification

method. For this reason, the numerical parameters assumed in the simulations done for this study all relate to ALTAIR and TRADEX.

7.2 TARGET SET SELECTION

Deciding which targets to observe during the data collection is based on not only their visibility to the radar site, but also their relative size and shape and their orbital and dynamical motion.

7.2.1 Target Shape and Size

The targets selected for the experiment should be of similar size and have shapes with either a known or calculatable RCS at the ALTAIR and TRADEX frequencies. Two of the target shapes used for the present contract are representative of existing calibration satellites* which could be included in the target set selected for the experiment. Expansion of the target set to include three or more existing satellites will require additional RCS data for the frequencies and polarizations of ALTAIR and TRADEX. If this data does not currently exist or for practical reasons cannot be measured, it would be obtained by calculation as was done for this report.

The space time integral equation method has been developed to a point where the scattering response of a large class of target shapes can be calculated. It has been used to compute the smoothed impulse response of smooth convex targets, targets with edges, thin wires, smooth convex bodies with wires attached, open thin surfaces, and cylinders with fins attached. In addition, this technique has been extended to the computation of the impulse response (entire frequency response) of smooth convex targets, targets with edges, rectangular plates and cylinders with fins attached. The applicability of the method is presently being increased further.

The cost of the experiment will depend on the complexity of the targets whose response is to be calculated. Detailed data concerning the

*For reasons of security classification, we will not elaborate on this correspondence.

shape and size of existing satellites must be examined in the light of the current or projected capabilities of the space-time integral equation method before the target set can be specified.

It is also likely that a meaningful test of the method will preclude using targets as similar in RCS as those assumed in this study because of the unavoidable one or two dB RCS calibration errors. Attempting to minimize this can greatly increase the cost of the experiment.

7.2.2 Target Dynamical Motion

The deliverable data items from KREMS are in many formats. The data cost can be greatly reduced if the so-called catalog or transcription tapes [4, 5, 16, 17] from ALTAIR and TRADEX are used for the experimental test of the classification method. These tapes contain RCS data at 40 observations per second for ALTAIR and 10 observations per second for TRADEX [16]. The RCS values are averages of the single pulse observations so that the observation rate must be consistent with the target aspect rate in order not to smear the target signature (that is, average pulses at significantly different target RCS). In this respect, the TRADEX Catalog tape will limit the maximum aspect rate because it averages RCS over a longer period of time (.1 seconds).

The effect of aspect changes on the apparent target RCS depends on the size of the target and the radar operating frequency. For large targets at high frequencies, only a small aspect change can result in a significant change in the RCS. This relationship can be quantified in an approximate way by considering a right circular cylinder tumbling end over end and viewed with a radar in the plane perpendicular to the axis of rotation (this is the worst case). The approximate RCS of a cylinder is [18]

$$\sigma(\phi) = \sigma_0 \left[\frac{\sin(kL \cos \phi)}{kL \cos \phi} \right]^2$$

where $k = 2\pi/\lambda$ is the radar wave number, ϕ is the aspect, L is the cylinder length and σ_0 is the broadside RCS. The width of the lobes in this scattering

pattern are $\lambda/2L$ radians. If the cylinder is rotating at Ω radians per second, $\lambda/(2L\Omega)$ seconds will be required for one entire lobe to evolve. If at least N observations are required to acceptably describe the RCS variation during this time, the radar observation rate, f_s , must satisfy

$$f_s \geq 4\pi N \frac{Lf}{cT} \quad (7-1)$$

where f is the radar frequency, c is the speed of light, and $T = 2\pi/\Omega$ is the tumble period. In this respect the TRADEX radar at S band (2950.8 MHz) demands the highest observation rate. On the Catalog tapes for TRADEX, $f_s = 10$, and equation (7-1) can be used to show acceptable tumble period -- target size pairs for a given value of N . Figure 23 shows the curve

$$T = \frac{4\pi N f}{c f_s} L,$$

for the S band TRADEX Catalog tape ($f_s = 10$) and $N = 10$ samples per lobe. Targets whose size and dynamical motion put them well under this curve should be excluded from the target set, not because of any limitation of the classification method, but because the Catalog tape has only ten observations per second.*

7.3 SPECIFIC DATA REQUIREMENTS

As indicated in Appendix 10.3, evaluation of the likelihood functions requires knowledge of the target range in addition to RCS measurements. Evaluation of the aspect estimation performance could be done for stabilized targets if azimuth and elevation measurements were also available.

In summary, the desired data from ALTAIR and TRADEX are target RCS at four frequencies and two receive polarizations as well as range, azimuth and elevation at the nominal Catalog tape rate for the major portion of at least one pass of each of the selected targets. As pointed out by Roth [3], data specifying the noise level in the receiver channels as well as the level of isolation between the cross-polarized channels must

* The use of MINOCM or instrumentation tapes would remove this restriction, but greatly increase the experiment cost.

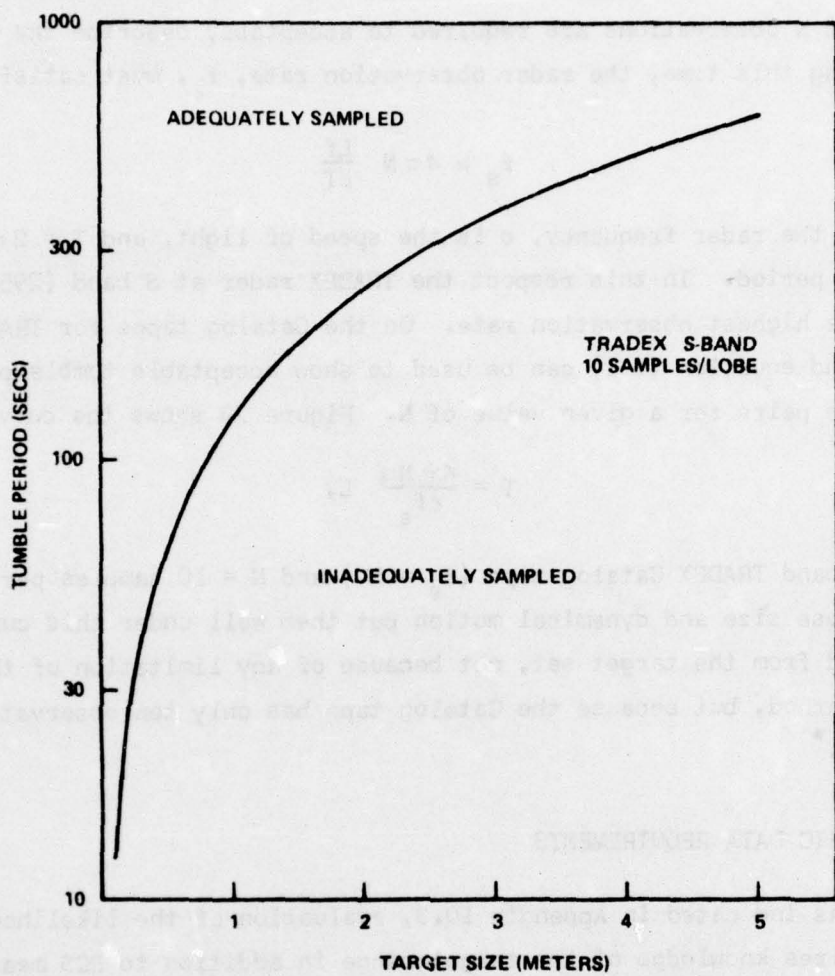


FIG. 23 Observation Rate Limitations for Tumbling Targets

be known.

7.4 IONOSPHERE EFFECTS

Since circular polarization is to be used, Faraday rotation will not be a problem. The effects of ionospheric scintillation [3, 14, 19], however, must be considered. If the classifier is not modified to account for this phenomenon as discussed in previous sections, there are two alternatives. The target set would be restricted to satellites with orbit altitudes less than 300 kilometers [3], or only data from periods of negligible ionospheric scintillation could be processed. The former procedure greatly reduces the number of candidate satellites for the target set and may not be feasible. The latter means that additional information about the existence of scintillation is required during the actual data collection so as to avoid rescheduling the exercise at a much later date.

SECTION 8
SUMMARY AND CONCLUSIONS

The objectives of this contract were to obtain the general expression for the impulse response of the prolate spheroid and sphere-capped cylinder as a function of arbitrary incident angle and polarization; to generalize the frequency space-trajectory classification technique to include unknown target aspect angle and polarization; to apply these results using the parameters of existing radars to demonstrate the decision process on a sphere, prolate spheroid, and sphere-capped cylinder of comparable size, including the effects of additive noise; and to plan experiments and determine which data would be needed to demonstrate the technique using real satellite data. The results discussed in the previous sections and in the attached appendices show that these objectives have been met or exceeded in every respect.

Several additional contributions were made during the course of the study. The classifier algorithm was developed from the foundation of statistical decision theory which not only provides excellent target classification performance, but also enables a more fundamental understanding of the importance of the various factors (for example radar system parameters) and operations (such as aspect estimation) which enter into any multifrequency classification scheme. The effect of the additive noise was realistically treated by modeling the radar receiver. The classifier was tested by simulating the motion of orbiting vehicles and the results show that early and reliable classification is achievable with this method. An advantage of the method is the automatic estimation of target aspect which could be used for target motion assessment. In addition, a measure of decision confidence as well as the capability to reject unknown targets were developed based on fundamental probabilistic considerations.

The major conclusion of this work is that the multifrequency approach to satellite object identification can be efficacious with operational radar technology. Only the data processing portions of existing

radar installations need be modified in order to apply the technique. In addition, because of the generality of the space-time integral equation method, a priori unknown or hypothetical target shapes can be identified without resorting to costly and tedious measurement techniques to form the signature library.

Future work on these ideas could include not only an experimental test as outlined in Section 7, but also further effort at extending the capabilities of the space time integral equation method to more complicated geometries. In addition, the classifier algorithm could be improved to include prior statistical information on target aspect variation and also the effects of ionospheric scintillation. The developments made in this study provide the fundamental foundations for these extensions within the precepts of the theory of statistical hypothesis testing. This work could result in the optimum (minimum probability of error) classifier and would be the standard against which competing methods are judged.

As indicated in the text of this report, no substantive effort was expended to minimize the computer resource requirements (storage and processing time) for the classifier. It is likely, however, that the implementation can be made very efficient. The parallel structure of the classifier (Figure 8) suggests the promising approach of using parallel micro-processor channels, each with its own small plug-in Read Only Memory (ROM). The target library could be modified by simply changing the ROMs.

SECTION 9
REFERENCES

1. A.A. Ksienki, Y. Lin, and L.J. White, "Low Frequency Approach to Target Identification," Proc. IEEE, Vol. 63 No. 12, December 1975, pp. 1651-1660.
2. W.B. Goggins, "Identification of Radar Targets by Pattern Recognition," Ph.D. Dissertation, Air Force Institute of Technology, Wright-Patterson AFB, Ohio, 1973.
3. This reference will be made available to qualified military and government agencies on request from RADC (OCTM) Griffiss AFB NY 13441.
4. ALTAIR Data Users Manual, Lincoln Manual 97, Volume I, Revision 3, 31 December 1975.
5. TRADEX Data Users Manual, Lincoln Manual 112, 1 March 1973.
6. M.I. Skolnik (ed.), Radar Handbook, McGraw-Hill, 1970.
7. H.L. Van Trees, Detection, Estimation and Modulation Theory, Part I, Wiley, 1968.
8. R.V. Hogg and A.T. Craig, Introduction to Mathematical Statistics, Macmillan, 1965.
9. A.D. Whalen, Detection of Signals in Noise, Academic, 1971.
10. R.R. Bate, D.D. Mueller, and J.E. White, Fundamentals of Astrodynamics, Dover, 1971.
11. B.L. Diamond and M.E. Austin, "The ARIES Program: Coordinates, Transformations, Trajectories, and Tracking," MIT Lincoln Laboratory Technical Note 1975-15, 5 September 1975.
12. C. Brindley, "Target Recognition," Space/Aeronautics, June 1965, pp. 62-68.
13. B.J. Burdick, "TUMBLE: A Dynamic Simulation Program," MIT Lincoln Laboratory Project Report RMP-54, 8 January 1975.
14. H.E. Whitney, "Ionospheric Scintillation Effects on VHF/UHF Communication Systems," AFGL-TR-76-0097, 3 May 1976.
15. R.A. Ross, "Investigation of Scattering Principles, Volume III -- Analytical Investigation," RADC-TR-68-340, May 1969. AD# 856560.

16. C.R. Berndtson, private communication.
17. Kwajalein Missile Range Instrumentation User Support Facilities Manual
18. D.K. Barton, Radar System Analysis, Prentice-Hall, 1964.
19. This reference will be made available to qualified military and government agencies on request from RADC (OCTM) Griffiss AFB NY 13441.
20. C.L. Bennett, "A Technique for Computing Approximate Electromagnetic Impulse Response of Conducting Bodies," Ph.D. Dissertation, Purdue University, Lafayette, Indiana, August 1968.
21. C.L. Bennett, J.D. DeLorenzo and A.M. Auckenthaler, "Integral Equation Approach to Wideband Inverse Scattering," Sperry Research Center, Sudbury, Mass., Final Report on Contract No. F30602-69-C-0332, June 1970. RADC-TR-70-177. AD#876849.
22. C.L. Bennett and R. Hieronymus, "Space-Time Integral Equation Approach to Solution of Plane Symmetric Scattering Problems," Sperry Research Center, Sudbury, Mass., Interim Report on Contract No. F30602-75-C-0040, May 1975. RADC-TR-76-59. AD#A023204.
23. R.M. Hieronymus and C.L. Bennett, "Space-Time Integral Equation Solution of Rotationally Symmetric Scattering Problems," Sperry Research Center, Sudbury, Mass., Interim Report on Contract No. F30602-75-C-0040, May 1975. RADC-TR-76-59. AD#A023204.
24. C.L. Bennett, K.S. Menger, R. Hieronymus et al, "Space-Time Integral Equation Approach for Targets with Edges," Sperry Research Center, Sudbury, Mass., Final Report on Contract No. F30602-73-C-0124, May 1974. RADC-TR-74-132. AD#785120/7GI.
25. R. Hieronymus and C.L. Bennett, "Space-Time Integral Equation Approach to Solution of Linear Thin-Wire Scattering and Antenna Problems," Sperry Research Center, Sudbury, Mass., Interim Report on Contract No. F30602-75-C-0040, May 1975. RADC-TR-76-59. AD#A023204.
26. C.L. Bennett and R.M. Hieronymus, "Space-Time Integral Equation Approach to Solution of Scattering Problems Involving Surfaces with Wires Attached," Sperry Research Center, Sudbury, Mass., Interim Report on Contract No. F30602-75-C-0040, May 1975. RADC-TR-76-59. AD#A023204.
27. C.L. Bennett, R.M. Hieronymus, and D. Peterson, "Integral Equation Solution," Sperry Research Center, Sudbury, Mass., Final Report on Contract No. F30602-75-C-0040, November 1975. RADC-TR-76-59. AD#A023204.
28. C.L. Bennett, A.M. Auckenthaler, R.S. Smith and J.D. DeLorenzo, "Space-Time Integral Equation Approach to the Large Body Scattering Problem," Sperry Research Center, Sudbury, Mass., Final Report on Contract No. F30602-71-C-0162, May 1973. RADC-TR-73-70. AD#763794.

29. D.L. Moffatt and E.M. Kennaugh, "The Axial Echo Area of a Perfectly Conducting Prolate Spheroid," IEEE Trans. Antennas and Propagation AP-13, 401-409, May 1965.
30. P.B. Patnaik, "The Non-Central χ^2 and F-Distributions and Their Applications," Biometrika, Vol. 36, 1949, pp. 202-232.
31. N.L. Johnson and S. Kotz, Continuous Univariate Probability Distributions, Vols. 1 and 2, Houghton Mifflin, 1970.

SECTION 10
APPENDICES

10.1 THE SPACE-TIME INTEGRAL EQUATION METHOD

The basis of most Satellite Object Identification (SOI) techniques is a signature library containing the characteristics of known targets. The measured characteristics of the radar signals scattered by the unknown object are then compared to this library of a priori known features. This signature library is obtained either by measurement or by theoretical calculation of the scattering response of objects. Until recently, fairly general but approximate computational methods were available only for the cases of target size much smaller (Rayleigh region) or much larger (optical region) than wavelength. These frequency regions are useful for describing the volume and projected area, respectively, of the target, but the appropriate frequency region for shape characterization is the resonance band where wavelength is of the order of target size. A generally applicable method for computing the scattering response of an object at all frequencies is the space-time integral equation method developed at the Sperry Research Center. With this technique, the target response due to any radar waveform, regardless of carrier frequency, can be computed.

The space-time integral equation method uses a two step approach to obtain the impulse (or equivalently, frequency) response of an object. First, the smoothed impulse response of the object is obtained by the solution of a space-time integral equation. This equation gives the currents flowing on the surface of the object from which the far field may be computed directly. The second step involves the application of the impulse response augmentation techniques. This technique combines the smoothed impulse response with the known singular contributions to the impulse response to obtain the total impulse response and the frequency response of the object at all frequencies.

10.1.1 SPACE-TIME INTEGRAL EQUATION SOLUTION

The space-time integral equation technique was developed in 1968 [20]. This powerful approach to the solution of transient electromagnetic scattering and radiation problems consists of formulating a time domain integral equation for the surface currents on the scatterer in such a way that the integral equation can be reduced to a recurrence relation in time, thus making matrix inversion unnecessary. This equation is then solved numerically for the surface currents, which, in turn, are used to compute the far field.

This technique has been applied to closed surfaces [21, 22, 23, 24] using an \vec{H} -field integral equation and to wires [21, 25] and open, thin surfaces [24] using an \vec{E} -field integral equation. In addition the method was applied to wires on bodies [21, 26] and fins on bodies [27] using a hybrid approach which applies an \vec{E} -field integral equation over one part of the target and an \vec{H} -field integral equation over the other.

For the cases of the prolate spheroid and the sphere-capped cylinder used in this SOI application the formulation for closed surfaces is used. The space-time integral equation for the surface current density is derived using an \vec{H} -field boundary condition, and is given by

$$\vec{J}(\vec{r}, t) = 2\hat{a}_n \times \vec{H}^i(\vec{r}, t) + \frac{1}{2\pi} \int_S \hat{a}_n \times \left[\frac{1}{R} + \frac{1}{Rc} \frac{\partial}{\partial \tau} \right] \vec{J}(\vec{r}', \tau) \times \hat{a}_R dS' \quad (10-1)$$
$$\tau = t - R/c$$

where

\vec{r} = position vector to the observation point on the surface

\vec{r}' = position vector to the integration point

$$R = |\vec{r} - \vec{r}'|$$

$$\hat{a}_R = \frac{\vec{r} - \vec{r}'}{R}$$

c = the speed of light

\hat{a}_n = the unit normal to the surface at \vec{r}

S = the surface.

The space-time integral equation in equation (10-1) represents, in principle, the complete solution of the general scattering problem for an excitation with arbitrary time dependence. However, in most practical scattering problems the incident field is a plane wave. This is the space variation which has been used to date, but it should be pointed out that the solution of the scattering problem for other space variations of the incident wave (e.g., a spherical incident wave) would be equally easy to implement.

For numerical solution of the space-time integral equation in equation (10-1), the incident wave was taken to be the standard Gaussian regularization of an impulse, namely

$$s_n(t) = \frac{n}{\sqrt{\pi}} e^{-n^2 t^2} \quad (10-2)$$

which converges to the delta functional as n goes to infinity. The time domain integral equation can be solved exactly for bodies with linear dimensions up to several pulse widths of this regularized impulse.

To implement the numerical solution the scattering surface is divided into curvilinear patches of approximately equal area with a space sample point at the center of each patch. The spacing of these sample points (and thus, the size of the patches) on the surface is chosen small enough to give both a good representation of the scatterer and also a good representation of the currents that exist on the scatterer. Next, the time increment Δt between the points in time at which the current is computed must be less than the time it takes a wave, moving at the speed of light, to travel between the closest space points. Satisfaction of this condition insures that equation (10-1) can be solved without resorting to a matrix inversion. Equation (10-1) is solved on a digital computer for the current density by simply marching on in time. Once the current density has been obtained, the far scattered field is computed.

10.1.2 Impulse Response Augmentation Technique

The impulse response augmentation technique, first suggested in 1968, [20] deals directly with the smoothed impulse response of targets in the far field. As described earlier, the smoothed impulse response is computed using the space-time integral equation approach and has yielded good results up to body sizes of several pulse widths or, equivalently, several wavelengths. The regions of slow variation in the smoothed impulse response remain the same in the exact impulse response; thus it is only necessary to determine the structure of the singular regions and any other regions of fast variation. But the singular portions of the exact impulse response that result from scattering by specular points on smooth convex targets can be computed exactly and hence do not need to be computed by solving the space-time integral equation. The impulse response augmentation technique combines the smoothed impulse response, the known singular contribution to the impulse response, and the theory of Fourier transforms to produce the total impulse response and the frequency response (system function) of the target at all frequencies.

The feasibility of accurately computing the total frequency response or the exact impulse response using the impulse response augmentation technique has been demonstrated [28] for the case of the sphere by comparing the computed responses with results obtained by classical solution of the boundary value problem in the frequency domain and performing the inverse Fourier transform. This technique has also been applied to the case of the prolate spheroid and has yielded results in good agreement with measurements and represents an improvement on the Moffatt-Kennaugh exponential sum approximation [28, 29].

In addition, results for the total impulse response and the frequency response over the entire spectrum have been obtained for the sphere-capped cylinder, the sphere-cap flat-end cylinder, the right-circular cylinder, the square flat plate and the cylinder with fins attached. Details of the augmentation technique and displays of the results obtained may be found in several references [24, 27, 28].

10.1.3 Application to Prolate Spheroid and Sphere-Capped Cylinder

The impulse response augmentation technique was applied to obtain the response of the prolate spheroid and the sphere-capped cylinder at an arbitrary aspect angle and polarization. The smoothed impulse responses of these targets were obtained using the space-time integral equation solution. The singular portions of the response were obtained by assuming physical optics currents on the scattering surface. This reduces the problem to the determination of the projected area function.

Using this approach, the effect of the singular portions of the impulse response of a prolate spheroid was expressed as

$$f_a(t) = P_z \delta(t/a - T_z) + (S_z + S_{z2})u(t/a - T_z) + R_{z2} r_p(t/a - T_z) \quad (10-3)$$

where

P_z = the impulse coefficient given by the physical optics approximation

S_z = the step coefficient given by the physical optics approximation

S_{z2} = the step coefficient due to the polarization dependence

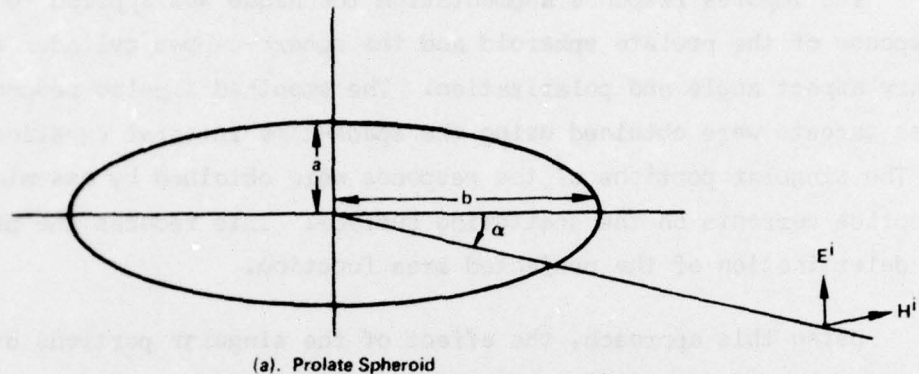
R_{z2} = the ramp coefficient due to the polarization dependence

T_z = the time at which the leading edge of the impulse response starts.

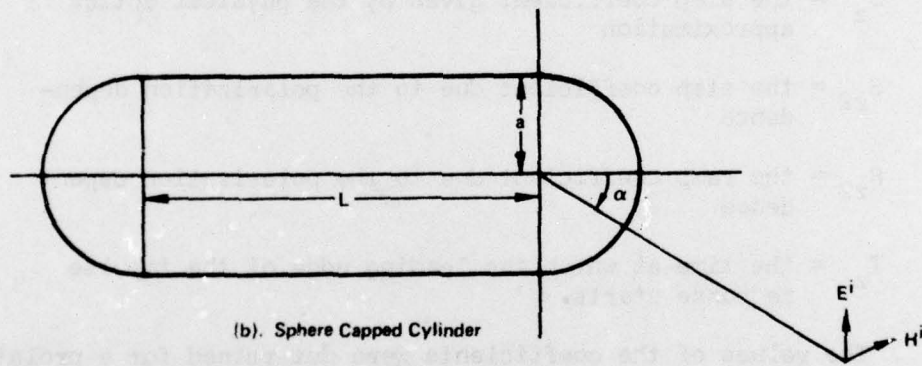
The values of the coefficients were determined for a prolate spheroid, shown in Figure 24(a), with semiminor axis a and semimajor axis b . The incident wave was assumed to make an angle α with the major axis. The resulting expressions were

$$T_z = -2 \frac{B^2}{a}^{\frac{1}{2}}$$

$$P_z = \frac{1}{2} \frac{ab}{B}$$



(a). Prolate Spheroid



(b). Sphere Capped Cylinder

FIG. 24 Geometries of Targets for Signature Library

$$S_z = -\frac{1}{4} \frac{a^2 b}{B^{3/2}}$$

$$B = a^2 \sin^2 \alpha + b^2 \cos^2 \alpha$$

The values of S_{z2} and R_{z2} were computed from the smoothed impulse response $r(t)$ initially in time by assuming that the total value of $r(t)$ is due to the convolution of $f_a(t)$ with the excitation $e(t)$. The values of S_{z2} and R_{z2} were then determined by equating $f_a * e$ with $r(t)$ at the initial time points in the smoothed impulse response and solving the resulting set of linear algebraic equations. Confidence in this approach was further strengthened by noting that the values of S_{z2} and R_{z2} were relatively independent of the particular time points used for their solution. The fit to $r(t)$ was made for a set of incident angles and then a parabolic fit to those values was used to determine the values of S_{z2} and R_{z2} for intermediate angles.

The same approach was also taken to obtain the response of a sphere-capped cylinder. The effect of the singular portions of the response was expressed as

$$\begin{aligned} f_a(t) = & P_1 \delta(t/a - T_1) + S_1 u(t/a - T_1) + A_2 (t/a - T_2)^{-\frac{1}{2}} u(t/a - T_2) \\ & + B_2 \exp\left(\frac{t/a - T_2}{P}\right) (t/a - T_2)^{-\frac{1}{2}} u(t/a - T_2) \\ & + A_3 (t/a - T_3)^{-\frac{1}{2}} u(t/a - T_3) \\ & + B_3 \exp\left(\frac{t/a - T_3}{D}\right) (t/a - T_3)^{-\frac{1}{2}} u(t/a - T_3) \end{aligned}$$

where

P_1 = the impulse coefficient due to the specular return

S_1 = the step coefficient due to the specular return

A_2, B_2 = the coefficients due to the first sphere-cap/cylinder join

A_3, B_3 = the coefficients due to the second sphere-cap/cylinder join

T_1 = the time of the specular return

T_2 = the time of the first join return

T_3 = the time of the second join return.

The values of the coefficients were expressed for a sphere-capped cylinder, shown in Figure 24(b), of radius a and length L . The incident wave was assumed to make an angle α with the axis of the cylinder. The resulting values of the coefficients were

$$P_1 = a/2$$

$$S_1 = -0.25$$

$$A_2 = \frac{a^{1/2} (\sin \alpha)^{3/2}}{2\pi \cos \alpha (1 + \sin \alpha)}$$

$$B_2 = -A_2$$

$$A_3 = -A_2$$

$$B_3 = A_2$$

$$D = 2a (1 - \sin \alpha)$$

$$T_1 = -2a$$

$$T_2 = -2a \sin \alpha$$

$$T_3 = -2a \sin \alpha + 2L \cos \alpha$$

Once the singular portions of the responses were determined, they were then combined with the computed smoothed impulse responses and the impulse response augmentation technique was applied. This yielded the impulse response of the target and, using the Fourier transform, the frequency response for any aspect angle and any polarization.

10.2 STATISTICS OF THE RCS MEASUREMENTS

Figure 25 is a model of a radar receiver which consists of a matched filter, square-law envelope detector, and a video pulse averager

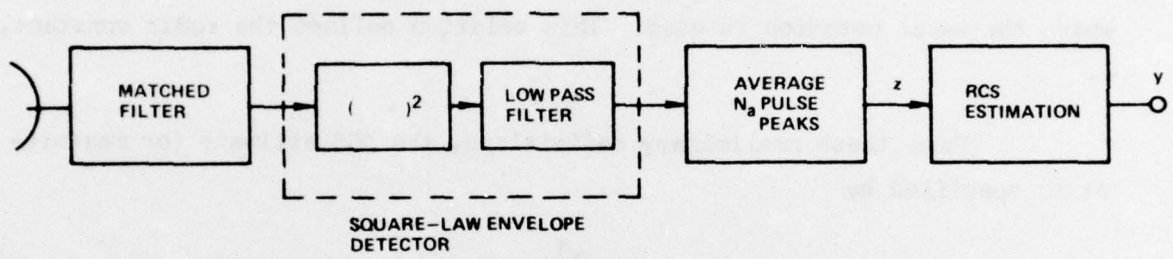


FIG. 25 Model of Radar Receiver

with output z . For a signal in Gaussian noise it can be shown [9] that $q = N_a z/W$ has a non-central chi-square distribution with $2N_a$ degrees of freedom and non-central parameter $\lambda = N_a \pi^2/W$ where W is the total noise power out of the matched filter, π^2 is the square of the peak signal envelope, and N_a is the number of pulses averaged to obtain z . The peak (squared) signal envelope is related to the target RCS by the radar equation

$$\pi^2 = \frac{2 P_t G^2 \lambda^2}{(4\pi)^3 L} \frac{\sigma}{R^4} = \frac{\gamma \sigma}{R^4} \quad (10-4)$$

where the usual notation is used. This relation defines the radar constant, γ .

From these preliminary definitions, the RCS estimate (or measurement) specified by

$$y = \frac{R^4}{\gamma} (z - 2W)$$

is unbiased. That is,

$$E(y) = \sigma = \text{true target RCS.}$$

It can also be shown that

$$\text{Var}(y) = \frac{4KR^4}{N_a} \left[\sigma + KR^4 \right]$$

where $K = W/\gamma$ is a constant of the radar.

The unbiased RCS estimate, y , is linearly related to the chi-square random variable, q , which has probability density [9]

$$p(q) = \frac{1}{2} \left(\frac{q}{\lambda} \right)^{\left(\frac{N_a}{2} - \frac{1}{2} \right)} I_{N_a-1} \left(\sqrt{q\lambda} \right) \exp \left(-\frac{\lambda}{2} - \frac{q}{2} \right); q \geq 0$$

where I_n is the modified Bessel function of order n . The RCS measurement y will therefore have a probability density of similar functional form.

The random RCS observations simulated for this study were generated by summing the square of $2N_a$ Gaussian random variables with means determined by the true target RCS, the appropriate radar constant K , and the target range R . This approach allowed exact simulation of the output of the system in Figure 25.

10.3 DETAILS OF THE LIKELIHOOD FUNCTIONS

As is evident from the discussion in Section 3, the function describing the probability density of the RCS observation, y , must be evaluated many times during the execution of the classification algorithm. This computational load can be greatly reduced if the Bessel function evaluations are eliminated by using an approximation to the probability density function (likelihood function) for y . This could be accomplished using the results of Patnaik [30], but we have chosen a simpler first-order approximation. As the degrees of freedom becomes large, the non-central chi-square distribution may be roughly approximated by the normal or Gaussian distribution [31].

With this approach, y is linearly related to the Gaussian variate, q , so that the approximate likelihood function for the RCS observation at frequency f_i is

$$p(y) = \left[\frac{N_a}{8\pi K_i R^4 (\sigma + K_i R^4)} \right]^{\frac{1}{2}} \exp \left[- \frac{N_a (y - \sigma)^2}{8K_i R^4 (\sigma + K_i R^4)} \right]$$

The approximate likelihood function for a multifrequency observation of target RCS will then be the multivariate Gaussian probability density function which is completely specified by its mean vector and covariance matrix. Since the random variability of the RCS measurements at different frequencies is produced by the noise in different receiver channels, the RCS measurements at different frequencies are statistically independent and the covariance matrix is diagonal. If Y is the vector* multifrequency

* T denotes the transpose of a matrix.

observation of target RCS

$$Y = \begin{bmatrix} y_1 & y_2 & \cdots & y_{N_f} \end{bmatrix}^T$$

where y_i is the RCS observation at frequency i , the approximate likelihood function for Y is

$$P(Y) = \frac{1}{(2\pi)^{N_f/2} |C|^{\frac{1}{2}}} \exp \left\{ -\frac{1}{2} (Y - M)^T C^{-1} (Y - M) \right\}$$

where the covariance matrix has diagonal elements

$$C_{ii}(\varphi) = \frac{4K_i R^4}{N_a} \left[\sigma_i(\varphi) + K_i R^4 \right]$$

and the mean vector has components

$$M_i(\varphi) = \sigma_i(\varphi)$$

Note that the last two equations make explicit the aspect, φ , dependence of the radar cross section and the subscript i is a frequency index. Although not indicated above, this likelihood function is different for different targets as manifested by the different sets of functions $\{\sigma_i(\varphi) : i = 1, 2 \dots N_f\}$.

Reducing the matrix algebra to component form, the approximate log-likelihood function for a single multifrequency radar observation of RCS, assuming that a specified target is present, is given by

$$L_k(y_1, y_2, \dots, y_{N_f}; \varphi) = -\frac{1}{2} \sum_{i=1}^{N_f} \left\{ \ln V_i(\varphi) + \frac{y_i - \sigma_i(\varphi)^2}{V_i(\varphi)} \right\}$$

$$\text{where } V_i(\varphi) = \frac{4K_i R^4}{N_a} \left[\sigma_i(\varphi) + K_i R^4 \right]$$

The generalized log-likelihood function is of identical form but φ is

replaced by $\hat{\phi}$, the maximum likelihood estimate of aspect. The multiple observation likelihood is the sum of the single-look functions as indicated in Section 3.7.

The radar constants for the ALTAIR and TRADEX radars (obtained from the data in references 4 and 5) are shown in the following table.

Radar	Frequency (MHz)	K (meter ⁻²)
ALTAIR	155.5	4.42×10^{-27}
ALTAIR	415.	7.19×10^{-28}
TRADEX	1320.	3.71×10^{-28}
TRADEX	2950.8	4.93×10^{-28}

Figure 26 shows the single pulse Signal to Noise Ratio (SNR) for a one square meter target as a function of range for all four operating modes of the ALTAIR/TRADEX system.

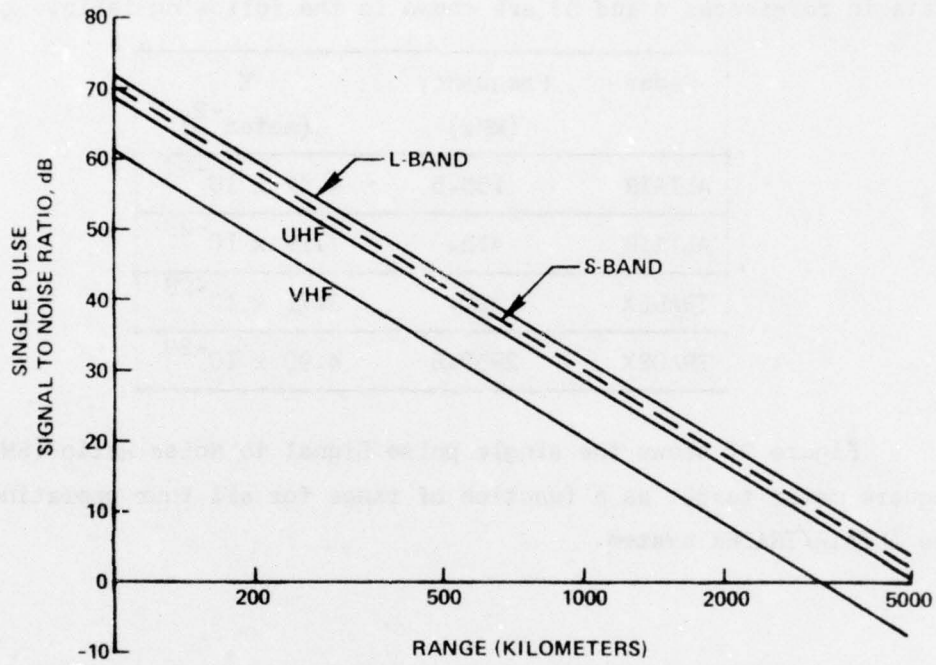


FIG. 26 Signal to Noise Ratio for One Square Meter Target

METRIC SYSTEM

BASE UNITS:

Quantity	Unit	SI Symbol	Formula
length	metre	m	...
mass	kilogram	kg	...
time	second	s	...
electric current	ampere	A	...
thermodynamic temperature	kelvin	K	...
amount of substance	mole	mol	...
luminous intensity	candela	cd	...

SUPPLEMENTARY UNITS:

plane angle	radian	rad	...
solid angle	steradian	sr	...

DERIVED UNITS:

Acceleration	metre per second squared	...	m/s
activity (of a radioactive source)	disintegration per second	...	(disintegration)/s
angular acceleration	radian per second squared	...	rad/s
angular velocity	radian per second	...	rad/s
area	square metre	...	m ²
density	kilogram per cubic metre	...	kg/m ³
electric capacitance	farad	F	A·s/V
electrical conductance	siemens	S	A/V
electric field strength	volt per metre	...	V/m
electric inductance	henry	H	V·s/A
electric potential difference	volt	V	W/A
electric resistance	ohm	...	W/A
electromotive force	volt	V	N·m
energy	joule	J	J/K
entropy	joule per kelvin	...	kg·m/s
force	newton	N	(cycle)/s
frequency	hertz	Hz	lm/m
illuminance	lux	lx	cd/m ²
luminance	candela per square metre	...	cd·sr
luminous flux	lumen	lm	A/m
magnetic field strength	ampere per metre	...	V·s
magnetic flux	weber	Wb	Wb/m
magnetic flux density	tesla	T	...
magnetomotive force	ampere	A	J/s
power	watt	W	N/m
pressure	pascal	Pa	A·s
quantity of electricity	coulomb	C	N·m
quantity of heat	joule	J	W/sr
radiant intensity	watt per steradian	...	J/kg·K
specific heat	joule per kilogram-kelvin	...	N/m
stress	pascal	Pa	W/m·K
thermal conductivity	watt per metre-kelvin	...	m/s
velocity	metre per second	...	Pa·s
viscosity, dynamic	pascal-second	...	m/s
viscosity, kinematic	square metre per second	...	W/A
voltage	volt	V	m
volume	cubic metre	...	(wave)/m
wavenumber	reciprocal metre	...	N·m
work	joule	J	

SI PREFIXES:

Multiplication Factors	Prefix	SI Symbol
$1\ 000\ 000\ 000\ 000 = 10^{12}$	tera	T
$1\ 000\ 000\ 000 = 10^9$	giga	G
$1\ 000\ 000 = 10^6$	mega	M
$1\ 000 = 10^3$	kilo	k
$100 = 10^2$	hecto*	h
$10 = 10^1$	deka*	da
$0.1 = 10^{-1}$	deci*	d
$0.01 = 10^{-2}$	centi*	c
$0.001 = 10^{-3}$	milli	m
$0.000\ 001 = 10^{-6}$	micro	μ
$0.000\ 000\ 001 = 10^{-9}$	nano	n
$0.000\ 000\ 000\ 001 = 10^{-12}$	pico	p
$0.000\ 000\ 000\ 000\ 001 = 10^{-15}$	femto	f
$0.000\ 000\ 000\ 000\ 000\ 001 = 10^{-18}$	atto	a

* To be avoided where possible.

MISSION
of
Rome Air Development Center

RADC plans and conducts research, exploratory and advanced development programs in command, control, and communications (C³) activities, and in the C³ areas of information sciences and intelligence. The principal technical mission areas are communications, electromagnetic guidance and control, surveillance of ground and aerospace objects, intelligence data collection and handling, information system technology, ionospheric propagation, solid state sciences, microwave physics and electronic reliability, maintainability and compatibility.

